Materials Today Bio 23 (2023) 100796

Contents lists available at ScienceDirect

Materials Today Bio

journal homepage: www.journals.elsevier.com/materials-today-bio

Nanomaterials-based precision sonodynamic therapy enhancing immune checkpoint blockade: A promising strategy targeting solid tumor

Xinlun Dai [a], Yangyang Du [b], Yumei Li [c,**], Fei Yan [b,*]

[a] Department of Hepatobiliary and Pancreatic Surgery, General Surgery Center, First Hospital of Jilin University, 71 Xinmin Street, Changchun 130021, China
[b] State Key Laboratory of Inorganic Synthesis and Preparative Chemistry, College of Chemistry, Jilin University, Changchun 130012, China
[c] Department of Pediatric Intensive Care Unit, First Hospital of Jilin University, 71 Xinmin Street, Changchun 130021, China

ARTICLE INFO

Keywords:
Nanoparticles
Sonodynamic therapy
Immune checkpoint blockade
Tumor microenvironment
Immunogenic cell death

ABSTRACT

Burgeoning is an evolution from conventional photodynamic therapy (PDT). Thus, sonodynamic therapy (SDT) regulated by nanoparticles (NPs) possesses multiple advantages, including stronger penetration ability, better biological safety, and not reactive oxygen species (ROS)-dependent tumor-killing effect. However, the limitation to tumor inhibition instead of shrinkage and the incapability of eliminating metastatic tumors hinder the clinical potential for SDT. Fortunately, immune checkpoint blockade (ICB) can revive immunological function and induce a long-term immune memory against tumor rechallenges. Hence, synergizing NPs-based SDT with ICB can provide a promising therapeutic outcome for solid tumors. Herein, we briefly reviewed the progress in NPs-based SDT and ICB therapy. We highlighted the synergistic anti-tumor mechanisms and summarized the representative preclinical trials on SDT-assisted immunotherapy. Compared to other reviews, we provided comprehensive and unique perspectives on the innovative sonosensitizers in each trial. Moreover, we also discussed the current challenges and future corresponding solutions.

1. Introduction

Various tumor treatments have emerged in the past few decades due to the vigorous advancement of nanotechnology [1]. Light-triggered modalities like PDT have exhibited desirable anti-tumor efficiency in several preclinical and clinical trials [2–4]. With the assistance of nano-delivery systems, photosensitizers can obtain a high tumor concentration and generate ROS, including singlet oxygen ($^1O_2$), hydroxyl radicals (•OH), or peroxyl radicals (•O_2H), to evoke tumor apoptosis or necrosis through proper irradiation [5–7]. Nevertheless, the low penetration ability of external light limited its application to certain superficial tumors [8]. SDT has been recently developed as a novel modality using ultrasound (US) as an excitation source and US-responsive substances as sonosensitizers to overcome such major drawbacks [9,10]. SDT shares similar principles with PDT but offers distinct advantages. Compared to the 10 mm depth of light, the US can achieve a sufficient penetration depth of up to 10 cm by adjusting frequency. In addition, the US does damage adjacent normal tissues even when applied with a high-intensity pattern, thereby exhibiting a better bio-safety profile towards laser irradiation [11,12] (Fig. 1). Thus, SDT possesses a promising therapeutic potential for deep-seated tumors by addressing conventional PDT shortcomings.

Despite the efforts to explore intrinsic mechanisms, the exhaustive ROS generation of sonosensitizers triggered by the US remains vague due to the complex procedures [13]. The acoustic cavitation-triggered son-mechanical/thermal damage and sonoluminescence-induced photochemical reaction provide the main explanations, followed by pyrolysis [14,15]. Besides the direct killing effect of ROS on tumors, studies have observed that SDT could enhance host immunity through the immunogenic cell death (ICD) process, similar to PDT [16,17]. The ICD refers to cell apoptosis, including the exposure and release of tumor-associated antigens (TAAs) and danger-associated molecular patterns (DAMPs), such as high-mobility group box-1 (HMGB1), calreticulin (CRT), heat shock proteins (HSPs), etc. [18]. The released TAAs and DAMPs can improve adaptive immunity function and reverse the immunosuppressive tumor microenvironment (TME) [19–22]. Nevertheless, the subsequent activation of multiple signaling pathways in tumors facilitates immune escape. For instance, the upregulation of inhibitory immune checkpoint ligands enables the tumors to gradually adapt to the new environment by weakening immune response [23–25]. Thus, SDT monotherapy can only limit tumor growth compared to

* Corresponding author.
** Corresponding author.
E-mail addresses: ym_li@jlu.edu.cn (Y. Li), feiyan@jlu.edu.cn (F. Yan).

https://doi.org/10.1016/j.mtbio.2023.100796
Received 3 July 2023; Received in revised form 24 August 2023; Accepted 11 September 2023
Available online 16 September 2023

Abbreviations

PDT	photodynamic therapy
NP	nanoparticle
SDT	sonodynamic therapy
ICB	sonodynamic therapy
ROS	reactive oxygen species
1O2	singlet oxygen
•OH	hydroxyl radicals
•O2H	peroxyl radicals
US	ultrasound
SL	sonoluminescence
ICD	immunogenic cell death
TAA	tumor-associated antigens
DDS	drug delivery system
TiO2	titanium dioxide
MOF	metal organic framework
Ce6	chlorin e6
ICG	indocyanine green
HB	hypocretin B
GSH	glutathione
PD-1	programmed cell death protein-1
PD-L1	programmed death ligand-1
CTLA-4	cytotoxic T lymphocyte protein-4
IDO	indoleamine2,3-dioxygenase
DC	dendritic cell
ICI	immune checkpoint inhibitors

achieving complete elimination and preventing distant metastasis or recurrence [26]. Immunotherapy can harness and boost innate and adaptive immunity to exert a potent anti-tumor immune response. Among the various immunotherapy types, ICB can reinvigorate exhausted effector T cells, induce dendritic cell (DCs) maturation, and downregulate Tregs proportion by affecting the interaction between the immunosuppressive immune checkpoints and their ligands [27–29]. Therefore, SDT-assisted immunotherapy combined with ICB therapy can provide a synergistic anti-tumor effect and elicit a long-term immune memory, thereby preventing tumor rechallenges.

Herein, we first described the current landscape of SDT and ICB therapy, respectively. Then we demonstrated the synergistic mechanism of the two strategies and summarized the up-to-date preclinical trials based on SDT + ICB (Table 1). Notably, we described multiple representative experiments and the unique design of the corresponding nanomaterials following the different types of sonosensitizers. Afterward, analysis and perspectives on the advantages or disadvantages of those nano-sonosensitizers were discussed. Finally, we describe the current issues and provide solutions enabling rapid clinical translation of such treatment modalities. The schematic illustration of the synergistic anti-tumor mechanism of NPs-based SDT combined with ICB therapy in this review was summarized in Fig. 2.

2. Current landscape of SDT

The ultimate therapeutic performance of SDT is multi-factorial, such as the selected tumor models, sonosensitizer species, applied US frequency and intensity, and specifically designed nanoplatforms [57]. Here, the mainstream ROS-generating SDT mechanism will be first introduced. Secondly, we will classify the sonosensitizers into organic and inorganic ones and hybrid crystalline porous polymers and summarize them. Then, we will review the primary defects of the current SDT and provide resolution through the typical nanomaterial modification or treatment schemes.

2.1. ROS generating mechanism

The intrinsic SDT mechanism under ultrasonic excitation remains unclean. However, there are three primary explanations: acoustic cavitation, sonoluminescence, and pyrolysis [58–61]. The physical phenomenon of acoustic cavitation is defined as the mechanical force exerted by US waves on microbubble generation in a liquid environment. The process involves nucleation, growth, and oscillation of gaseous cavities [62]. Cavitation is classified into two forms: stable and inertial. Stable cavitation is the stable oscillation of bubbles without

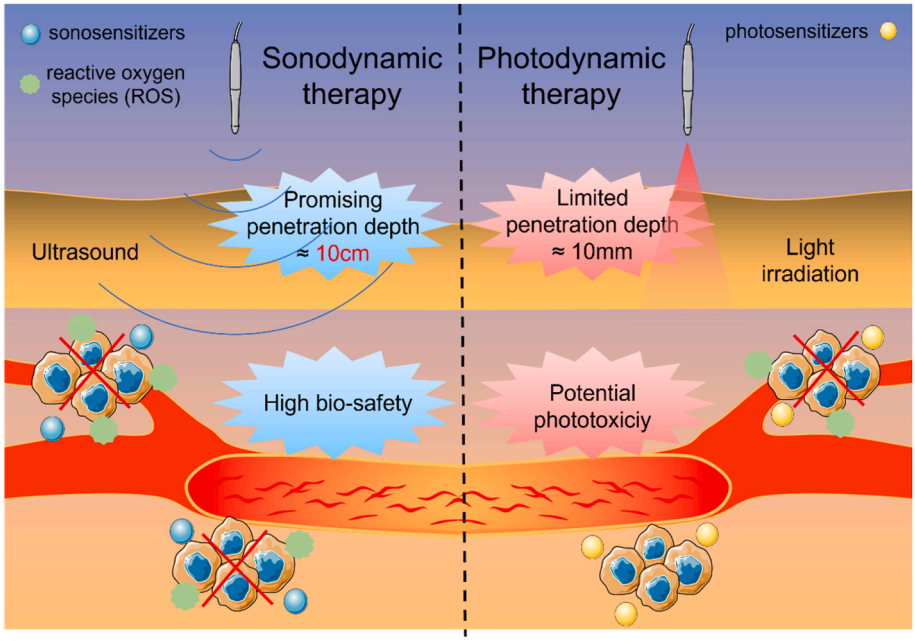

Fig. 1. The schematic illustration provides the basic concept and advantages of SDT over traditional PDT.

Table 1
Summary of pre-clinical trials of nanoparticles-assisted sonodynamic immune checkpoint blockade therapy.

Materials Type	Nanomaterials	Sonosensitizers	US parameters	Characteristics or modification	Immunotherapy	Tumor type	Ref.
Organic	HMME/R837@Lip (intravenously injected)	Hematoporphyrin monomethyl ether (HMME)	1 MHz, 1.5 W/cm^2, 5 min	Main components are FDA-approved agents	Immune adjuvant (R837) (conjugated) & *anti*-PD-L1 antibody (intraperitoneally injected)	4T1, CT26 tumor cells	[30]
	CHINPs (intravenously injected)	HMME	1 MHz, 2 W/cm^2, 5 min	PTT & multimodal imaging & 4T1 cell membrane coating	*Anti*-PD-1 antibody (intraperitoneally injected)	4T1 tumor cells	[31]
	PFCE@THPPpf-COPs (intratumorally injected)	4-hydroxylphenyl porphyrin	40 kHz, 2 W, 30 min	Perfluorocarbons (PFC) induced tumor hypoxia attenuation	*Anti*-CTLA-4 antibody (intratumorally injected)	CT26 tumor cells	[32]
	PMPS (intravenously injected)	Protoporphyrin IX	3 MHz, 1 W/cm^2, 5 min	Endoplasmic reticulum targeting & tumor vascular targeting	*Anti*-PD-L1 antibody (Intraperitoneally injected)	PanC02 tumor cells	[33]
	iCRET (intravenously injected)	verteporfin	1 Hz, 5.0 W, 8 min	Chemiluminescence resonance energy transfer (CRET)-based SDT: ROS amplification & CO_2 generation	*Anti*-PD-1 antibody (Intraperitoneally injected)	CT26, 4T1-Luc tumor cells	[34]
	PFP@PEG-CMD-Ce6	Chlorin e6 (Ce6)	1.5 MHz, 10 W, 10 min	RIPK3-independent necroptosis via inducing burst-mediated cell-membrane disintegration	*Anti*-PD-L1 antibody	CT26 tumor cells (RIPK3-deficient)	[35]
	CPDA@PFH (intratumorally injected)	Ce6	500 Hz, 3min	Ultrasonic-Thermal Effect	*Anti*-PD-L1 antibody (intravenously injected)	4T1 tumor cells	[36]
	P-aPD-L1/C (intravenously injected)	Ce6	2 MHz, 2.0 W/cm^2, 5 min	pH and MMP-2 dual-sensitivity	*Anti*-PD-L1 antibody (conjugated)	B16F10 tumor cells	[37]
	MFC (intravenously injected)	Ce6	1.0 MHz, 2.0 W/cm^2, 3 min	Tumor cell coating & Fe-PDAP based "H_2O_2 economizer"-mediated on-demand O_2 evolving process	*Anti*-PD-1 antibody (intraperitoneally injected)	4T1, Panc-1, HepG2, SKOV3 tumor cells	[38]
	sPD-1/Ce6-NBs (intravenously injected)	Ce6	1.1 MHz, 1.8 W/cm^2, 2 min	Nanobubbles-induced necrosis & sPD-1 transfection	Soluble PD-1 (incubated with Ce6-NBs)	H22 tumor cells	[39]
	HB-NLG8189@MPCM (intravenously injected)	HB (Ce6–C15-ethyl ester)	1 MHz, 1.25 W/cm^2, 10 min	Macrophage membrane coating	IDO inhibitor (NLG8189) (Self-assembly)	4T1 tumor cells	[40]
	Lip-ICG-PFP-cRGD (intravenously injected)	Indocyanine green (ICG)	2 W/cm^2, 10 min	Perfluoropentane (PFP) based 'nanobomb' induced necrosis	*Anti*-PD-1 antibody (intraperitoneally injected)	TC-1 tumor cells	[41]
	PIMS (intravenously injected)	IR780	1 MHz, 2.5 W/cm^2, 5 min	pH-responsive Mn^{2+} targeting cGAS-STING pathway for DCs activation	*Anti*-PD-L1 antibody (intravenously injected)	4T1 tumor cells	[42]
	TIR@siRNA (intratumorally injected)	IR780	1 MHz, 2 W/cm^2, 5 min	Nucleus-targeting ability of TAT peptide & Nrf2 down regulation	DPPA-1 peptide (*Anti*-PD-L1) (intravenously injected)	CT26 tumor cells	[43]
	MLipRIR (intravenously injected)	IR780	1 MHz, 1.5 W/cm^2, 5 min	Mitochondrial-targeting & R162 induced glutathione peroxidase downregulation	*Anti*-PD-L1 antibody (Intraperitoneally injected)	4T1 tumor cells	[44]
	Tf@IR820-DHA (intravenously injected)	IR820	40 kHz, 0.4 W/cm^2, 5 min	Fe (III)-mediated programmable catalysis of DHA	*Anti*-PD-L1 antibody (Intraperitoneally injected)	Hep1-6 tumor cells	[45]
	SPNAb (intravenously injected)	Semiconducting polymer	1 MHz, 1.5 W/cm^2, 5 min	$^1O_2$-cleavable linker modification	*Anti*-CTLA-4 antibody (conjugated)	4T1 tumor cells	[46]
	SPINs (intravenously injected)	Semiconducting polymer	1 MHz, 1.2 W/cm^2, 10 min	$^1O_2$-cleavable linker modification	IDO inhibitor (NLG919) & *anti*-PD-L1 antibody (conjugated)	Panc02 tumor cells	[47]
	MRP (intratumorally injected)	Methylene blue (MB)	40 kHz, 6.5 W/cm^2, 10 min	Glutathione-sensitive disulfide bonds linking Leu-MB and R837	Immune adjuvant (R837) & *anti*-PD-L1 antibody (intravenously injected)	CT26 tumor cells	[48]
	O_2MB-RB (intravenously injected)	Rose Bengal	1 MHz, 3.5 W/cm^2, 30 min	Rose Bengal conjugated microbubbles	*Anti*-PD-L1 antibody (intraperitoneally injection)	T110299 tumor cells	[49]
Inorganic	TiO2@CaP (intratumorally injected)	TiO_2	3 MHz, 2.1 W/cm^2, 10 min	Transformable design & Ca^{2+} induced mitochondrial dysfunction	*Anti*-PD-1 antibody (intraperitoneally injected)	4T1 tumor cells	[50]
	SCN@ B16F10 M/PEG-aPD-L1 (intratumorally injected)	TiO_2	1 MHz, 3 W/cm^2, 5 min	Melanoma cell membrane (B16F10 M) coating & aPD-L1 dual targeting effect	*Anti*-PD-L1 antibody (conjugated)	B16F10 tumor cells	[51]
	BMT@LA (intratumorally injected)	Black TiO_2	1 MHz, 1.5 W/cm^2, 5 min	L-arginine induced NO gas therapy	*Anti*-PD-L1 antibody (intravenously injected)	U14 tumor cells	[52]

(*continued on next page*)

Table 1 (*continued*)

Materials Type	Nanomaterials	Sonosensitizers	US parameters	Characteristics or modification	Immunotherapy	Tumor type	Ref.
	TiO_2–Ce6-CpG (intratumorally injected)	TiO_2, Ce6	1 MHz, 2 W/cm^2, 7 min	Dual sensitizer augment ROS quantum yield	Immune adjuvant (CpG ODN) & *Anti*-PD-L1 antibody (intravenously injected)	Hep1-6 tumor cells	[53]
	N@CAu-BMSNs (intravenously injected)	AuNPs	1 MHz, 1 W/cm^2, 3 min	Macrophage membrane coating & CO gas therapy induced mitochondrial dysfunction	IDO inhibitor (NLG919) (intraperitoneally injected)	4T1 tumor cells	[54]
	CFP (intravenously injection)	$CoFe_2O_4$	1 MHz, 1 W/cm^2, 5 min	Co^{2+}/Co^{3+} and Fe^{2+}/Fe^{3+} can render Fenton-like reaction	*Anti*-PD-L1 antibody (intraperitoneally injected)	4T1 tumor cells	[55]
	Zr-TCPP(TPP)/R837@M (intravenously injection)	Zr-MOF	3 MHz, 1.5 W/cm^2, 1 min	Mitochondrial-targeting by triphenylphosphonium (TPP) modification & 4T1 cell membrane coating	Immune adjuvant (R837) (loaded) & *Anti*-CTLA-4 antibody (intravenously injected)	4T1 tumor cells	[56]

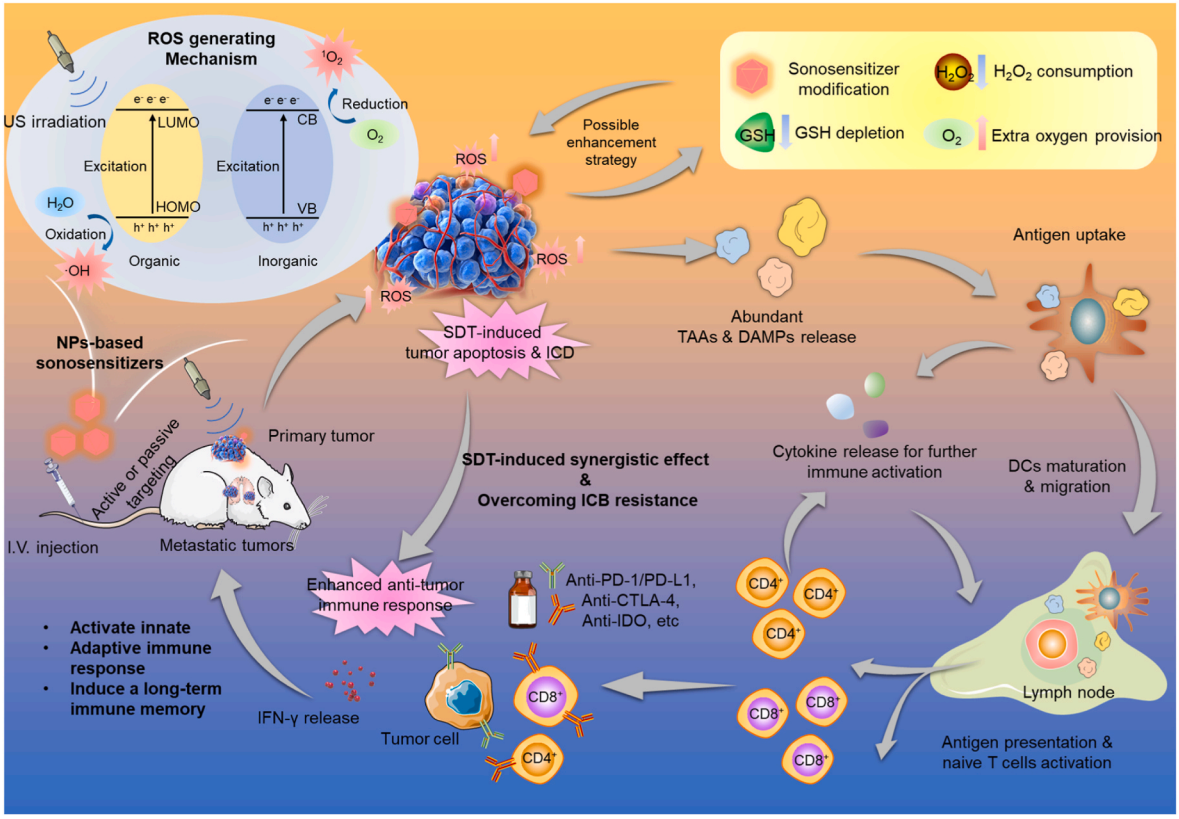

Fig. 2. The schematic illustration of the synergistic anti-tumor effect of NPs-based SDT combined with ICB therapy.

collapse, usually utilized for diagnostic purposes. While inertial cavitation indicated the rapid growth and violent rupture of bubbles. The microbubble collapse during inertial cavitation can lead to son-mechanical/thermal effects by generating shearing stress and high-temperature shockwaves within the surrounding microenvironment [63]. The harsh condition can cause severe damage to tumors by destroying the integrity of the cell membrane and enabling intracellular transport of agents. Moreover, the energy released during inertial cavitation can lead to a very short luminescence period, also called sonoluminescence (SL). The SL-based photochemical reaction is one of the most important mechanisms. The light emitted through SL is similar to the external irradiation incorporated in PDT. This can facilitate the photoactive sonosensitizers with related excitation wavelengths to transfer optical energy to oxygen molecules or other substrates within the surrounding area and produce ROS such as $^1O_2$. Additionally, the rapid temperature elevation through bubble collapses can cause sonochemical reactions to create free radicals and produce ROS, either by sonosensitizer pyrolysis or reacting sonosensitizers with water thermolysis products. With sufficient ROS presence in tumors, apoptosis-related physiological processes are initiated, including DNA fragmentation, mitochondrial dysfunction, and cell membrane damage [64–67]. The combination of the three processes elicits the tumor-killing SDT effect.

2.2. NPs-based sonosensitizers

Although acoustic cavitation can provide various energy forms, photoactive sonosensitizers are among the most frequently used molecules for SDT through SL [11,68,69]. Meanwhile, the constant research into NPs has contributed significantly to developing sonosensitizers. The application of nanomaterial-based drug delivery systems (DDS) or sonosensitizers can offer the following advantages over traditional ones: 1) promote sonosensitizer accumulation in tumors to improve therapeutic effect and reduce off-target effect through enhanced penetration retention or active targeting modifications [70,71]. 2) extend blood circulation time through tumor cell membrane camouflage or enhance

hydrophobic properties [72,73]. 3) achieve controllable drug release rather than "always-on" property through TME-responsive modifications [74–76]. 4) improve tumor-killing efficacy of combination treatment by carrying other drugs or displaying extra therapeutic effects [77,78]. 5) some inorganic nanomaterials can provide real-time diagnosis through various imaging strategies [79–81]. Herein, sonosensitizers can be divided into three major categories: 1) the small molecule organic semiconductors, extensively used as photosensitizers, including porphyrin derivatives [82,83] and cyanine derivatives [84,85]. 2) the inorganic semiconductors exhibit photocatalytic features, with transition metal oxides such as titanium dioxide (TiO_2) NPs [86–89], ZnO_2 NPs [90,91], and composite semiconductors doping Au [92], Ag [93] and Pt [94]. 3) the organic-inorganic hybrid ones, such as metal-organic framework (MOF)-derivatives [95,96]. They all have advantages and defects which can be selected for appropriate implementation.

2.2.1. NPs-assisted organic sonosensitizer

Upon US irradiation, the optical energy emitted can excite an organic sonosensitizer through SL when the electrons jump from the highest occupied molecular orbital (HOMO, bonding π orbitals) to the lowest unoccupied one (LUMO, anti-bonding π* orbitals) by absorbing more significant energy photons than the energy gap. Then, electronic charge transport could achieve a short-lived excited state and generate ROS by reacting with surrounding biological substrates, such as oxygen, after returning to the ground state. Based on the mechanism, better π-orbital overlap structure designs or increased π-π stacking have improved optoelectronic properties. Currently, traditional small molecule-based organic photoactive semiconductors are in the majority. Since Yumita et al. first reported hematoporphyrin as a desirable sonosensitizer in 1989, the porphyrin-derivatives, such as hematoporphyrin, protoporphyrin, hematoporphyrin monomethyl ether, and sino-porphyrin sodium, represent the most used organic sonosensitizers with high SDT efficiency [97]. Other derivatives, such as Ce6 and rose bengal (RB), have also demonstrated promising photocatalytic performance and intrinsic optoelectronic properties under specific US patterns [98–100]. Moreover, indole derivatives, such as ICG and IR780, have similar ROS-producing efficacy in SDT as in PDT [101,102]. These organic semiconductors share similar delocalized π-electrons in varied aromatic structures, yielding excellent optical properties and modification versatility. However, skin sensitivity, poor aqueous solubility, rapid metabolism, and the "always-on" effect affect their clinical application [103]. Furthermore, inadequate organic sonosensitizer accumulation in tumors leads to ROS deficiency and possibly self-destruct under oxidizing conditions [104]. NPs serving as DDS with satisfactory biocompatibility can provide ample drug-loading space and tumor-targeting ability to enrich sonosensitizers inside tumor regions [71]. Simultaneously, appropriate surface modification of NPs can prolong the circulation time and demonstrate the controllability of TME-responsive organic sonosensitizer. For instance, Wu et al. fabricated a silica-based biodegradable nanoplatform (CSI) loaded with catalase and ICG to exert SDT for glioblastoma [9]. Based on the penetrable ability of macrophages to cross the blood−brain barrier, CSI is coated with AS1411 aptamer-modified macrophage exosomes, providing excellent tumor-targeting capability. This intelligently designed nano-DDS significantly improves SDT efficacy by increasing tumor sonosensitizer concentration while relieving hypoxia by depleting glutathione and releasing oxygen.

2.2.2. Inorganic nano-sonosensitizer

Unlike organic ones, the inorganic semiconductors separate electrons (e^-) and holes (h^+) after absorbing optical energy upon the US. Then, the free e^- reacts with oxygen-related substances and generates ROS. The appropriate bandgap between the valence band (VB) and conduction band (CB) indicated the difficulty of excitation and recombination of the separated pairs. Thus, tremendous effects have been channeled on refining internal nanostructure, such as doping metal or fabricating heterojunctions to narrow bandgap or improve charge separation [105,106]. The abundant nucleation sites supplied by inorganic semiconductor nanostructure through the cavitation mechanism can form more bubbles. Thus, the extra explosion and pressure change within internal electronic fields continuously produces additional ROS. Due to the inherent chemical nature, inorganic sonosensitizers depict superior physicochemical properties than organic ones and are unaffected by photobleaching caused by the irreversible disruption of the chemical structure [26]. Moreover, minimal potential phototoxicity and skin sensitivity are associated with inorganic sonosensitizers, improving the safety profiles. Among the inorganic sonosensitizers, TiO_2 is representative due to its desirable photocatalytic nature, biological inertness, easy synthesis, and ready fabrication [107,108]. Other than TiO_2 NPs, silicon NPs [109], MOFs [110], black phosphorus [111] and noble metal-based inorganic sonosensitizers [112] are burgeoning with high ROS-generating potency. However, most metal-based sonosensitizers exhibited low ROS quantum yield (QY), needing additional modifications, such as incorporating comprised structures or metal coordination with organic sensitizers. For instance, Wang et al. designed a TiO_{1+x} nanorod using a typical organic-phase synthesis strategy [113]. This oxygen-deficient NR structure could serve as a charge trap to prevent the fast recombination of electrons (e^-) and holes (h^+), significantly enhancing ROS production. Moreover, the PEG−TiO_{1+x} NRs have potent nanozyme activities to elicit a combinational son/chemodynamic effect. Additionally, the undegradable nature of inorganic semiconductors limited their applications in biomedicine, demanding modification to enhance dissociation.

2.2.3. Hybrid sonosensitizer

MOFs, as a representative class of organic-inorganic hybrid sonosensitizers, can overcome the limitations of the former two types. The unique structure attributes render MOFs flexible roles in SDT. Under the US, the organic ligands absorb energy and activate metal ions/clusters to develop ROS through a linker-to-metal charge transfer mechanism. Additionally, the periodic array structure helps minimize self-quenching and promotes SDT efficiency [114]. Currently, porphyrin-ligand and Ti-based MOFs are two categories with strong sonodynamic effects and good biocompatibility [96,115].

2.3. Current challenges of NPs-based SDT and improvement strategies

Although the application of NPs significantly enhances the tumor accumulation and biocompatibility of sonosensitizers, the actual SDT therapeutic outcome is determined by many factors. Firstly, the low ROS QY of most sonosensitizers can seldom provide a desirable tumor-killing effect [116]. The obstinate TME negatively influences SDT, such as hypoxia, excess glutathione (GSH), overproduced hydrogen peroxide, etc. [117–119]. SStudies have observed that GSH is crucial in mediating the REDOX balance in cells and is closely associated with cancer development. Moreover, high GSH levels in tumors can hinder various cancer treatment strategies like SDT [120]. Furthermore, increasing intracellular antioxidants, such as catalase and Nrf2, can facilitate the tumors in evading oxidative stress [121,122]. Thus, various strategies have been developed to overcome the dilemmas, and we summarized them into four categories: 1) improve the ROS QY, such as developing new sensitizers, modifying NPs by adjusting the bandgap energy, or comprising metal coordination [106,123]. 2) relieve the hypoxia of TME or provide an extra oxygen source [124,125]. 3) weaken the intracellular antioxidant defense by depleting the GSH level [126]. 4) combining other strategies, such as radiotherapy, chemotherapy, gas therapy, and immunotherapy [127–129]. Immunotherapy, including cancer vaccines, ICB therapy, and adoptive T-cell therapy, is promising for advanced tumor treatment. Remarkable clinical outcomes have been achieved by applying ICB to boost the host systemic immune response and trigger immune cell activation [130]. More importantly, ICB therapy has also demonstrated an ideal therapeutic effect against metastasis

and recurrence in various tumor types [131–133]. Herein, we review the combination of NPs-mediated SDT assisting ICB therapy.

3. ICB therapy

The immune system serving as an "overseer" and "scavenger," can recognize and clean the malignant cells inside human bodies [134]. However, tumors have evolved immune escape mechanisms and developed an immunologically "cold" TME with exhausted immune cells [135,136]. Notably, tumor immune evasion mainly depended on the tumor or immune cell-induced overexpression of inhibitory immune checkpoint molecules. This included programmed cell death protein-1 (PD-1)/programmed death ligand-1 (PD-L1), cytotoxic T lymphocyte protein-4 (CTLA-4), and indoleamine2,3-dioxygenase (IDO) [137–139]. In TME, TAAs are presented to T cells by antigen-presenting cells, such as DCs, regulating the first co-stimulatory signal for T cell proliferation. The second antigen-independent signal transmitted through the bond between immune checkpoints determines the extent of immune activation. Under normal circumstances, cytotoxic $CD8^+$ T cells infiltrate and eliminate tumor cells as most of the adaptive immune response. In contrast, $CD4^+$ T cells secrete pro-inflammatory cytokines to improve host immunity. However, binding these inhibitory immune checkpoint receptors can trigger a "brake" signal for T cell activation and facilitate Tregs proliferation simultaneously [140]. Therefore, blocking their interaction can reinvigorate T cell function and boost tumor clearance. The FDA has approved multiple immune checkpoint inhibitors (ICIs) for clinical applications with outstanding therapeutic effects and prolonged progression-free survival among patients. These include Pembrolizumab (Keytruda) for non-small cell Lung cancer, Nivolumab (Opdivo) for hepatocellular carcinoma, and Ipilimumab (Yermoy) for advanced melanoma [141–143]. Apart from the classically FDA-approved antibodies, a series of novel small molecular ICIs and other checkpoints are being developed, including LAG3, TIGIT, TIM3, and B7H3, which are under investigation [144]. Herein, we focus on the role of PD-1/PD-L1, CTLA-4, and IDO.

3.1. PD-1/PD-L1 pathway

Programmed cell death protein-1 (PD-1), also called CD279, is a 55 kDa transmembrane protein expressed on immune cells, including activated lymphocytes (particularly on tumor-specific T cells), dendritic cells (DCs), macrophages, and natural killer cells. PD-1 maintains the self-tolerance balance by regulating T cell activation and inhibiting Treg cell apoptosis [145,146]. PD-1 ligand (PD-L1) is a transmembrane glycoprotein mainly found on lymphocytes, DCs, macrophages, or tumor cells [147]. Notably, the PD-L1 expression level on multiple tumors can be up-regulated in response to the pro-inflammatory factors triggering T-cell anergy, which is strongly associated with distant metastasis and poor prognosis [148]. The ligation of PD-1 and PD-L1 can cause an inferior T-cell response or even exhaustion in TME through TCR signaling impairment. Therefore, inhibiting the PD-1 and PD-L1 interaction with antibodies indicated a remarkable effector T cell activation and distinct tumor regression within multiple tumor types, including HCC, renal cell carcinoma, and non-small cell lung cancer [149]. Currently, there are six FDA-approved clinically used antibodies for PD-1/PD-L1 blockade. These are nivolumab (Opdivo, *anti*-PD-1), pembrolizumab (Keytruda, *anti*-PD-1), cemiplimab (Libtayo, *anti*-PD-1), durvalumab (Imfinzi, *anti*-PD-L1), atezolizumab (Tecentriq, *anti*-PD-L1), and avelumab (Bavencio, *anti*-PD-L1) [150]. Recently, Gogishvili et al. demonstrated a double-blind, placebo-controlled, phase 3 study examining cemiplimab plus platinum-doublet chemotherapy as first-line treatment against advanced NSCLC [151]. Four hundred sixty-six patients were recruited and randomized to receive corresponding measures (2:1). A strong efficacy indicated that the median OS of patients receiving ICI combining therapy was 21.9 months vs. 13.0 months in mono-chemotherapy patients. However, 43.6% of patients had Grade $\geq$3 adverse events with anemia and neutropenia, necessitating a better safety profile. Besides, antibodies and other ICIs targeting different tumors are undergoing clinical trials [152].

3.2. CTLA-4 pathway

Cytotoxic T lymphocyte protein-4 (CTLA-4) is expressed on Tregs and is responsible for averting autoimmune disorders by inducing T cell anergy by competing with its homolog CD28 [153]. The CTLA-4 pathway is quite distinct from PD-1 and mainly controls the function and proliferation of $CD4^+$ T cells by directly regulating effector T-cell response. Various studies have observed that the high level of CTLA-4 in Tregs is significantly associated with tumor progression and poor prognosis [154,155]. Moreover, CTLA-4 can enhance IL-2 production of $CD4^+$ T cells to elicit inhibitory function against immune response [156]. The CTLA-4 pathway blockade with antibodies attributed tumor regression with durable $CD4^+$ and $CD8^+$ T cell expansion by reducing Tregs. Currently, Ipilimumab (Yermoy) is the only FDA-approved CTLA-4 antibody against advanced melanoma [157], Tremelimumab (Imjudo) is another FDA-approved CTLA-4 antibody for a combination regimen with durvalumab targeting unresectable HCC depending on NCT02519348 and NCT03298451 [158]. The two studies revealed that patients treated with the single tremelimumab regular interval durvalumab (STRIDE) protocol ($n = 393$) showed a 22% lower death risk compared with sorafenib ($n = 389$). The STRIDE group median OS was 16.4 months (95%CI, 14.2–19.6) compared to 13.8 months in the sorafenib group (95%CI, 12.3–16.1). Other ICIs targeting CTLA-4 are undergoing clinical trials [159].

3.3. Ido pathway

Indoleamine 2, 3-dioxygenase 1 (IDO) is a rate-limiting enzyme expressed by mature DCs and tumors. IDO can induce immune cell inhibition or facilitate effector T cell apoptosis by metabolizing the essential amino acid tryptophan into downstream kynurenines [160]. Several IDO inhibitors have been developed recently, although none are currently approved for clinical use [161]. Zhai et al. summarized the ongoing and historical clinical trials targeting IDO [162].

3.4. Drug resistance in ICB

The ICB strategy has conferred unprecedented clinical benefits across various tumor types and revolutionized tumor immunotherapy. Despite the remarkable therapeutic outcome, only a small percentage of patients could benefit from ICI monotherapy. For instance, Zhu et al. reported an objective response rate of 17% in 104 advanced hepatocellular carcinoma patients receiving only Pembrolizumab in a non-randomized, multicenter, open-label, and phase II trial (KEYNOTE-224). The unsatisfactory benefit rate was likely due to the notorious drug resistance. ICI resistance can be categorized into two types according to mechanisms: primary resistance in patients with no initial response and acquired resistance in treatment or after discontinuation. The former is primarily attributed to genetic defects, epigenetic alterations, and low neoantigen expression [163]. For instance, Liu et al. observed that the KRAS-G12D mutation in NSCLC leads to inferior efficacy by decreasing PD-L1 levels and $CD8^+$ T cells [164]. Combining paclitaxel, a chemotherapeutic agent, with ICIs, could upregulate the HMGA2 level, thereby relieving KRAS-G12D-mutantion-caused resistance in NSCLC. Other factors may lead to ICI primary resistance, including IFN-γ signaling pathway disruption and inferior MHC-I expression in melanoma and NSCLC [165,166]. In contrast, the acquired one is more associated with intrinsic factors in immunosuppressive TME, such as low infiltration of lymphocytes, hyperactive abnormal angiogenesis, and overwhelming immunosuppressive cells and cytokines in TME [167,168]. Firstly, the inferior lymphocyte recruitment is partially attributed to insufficient antigen production and presentation. Hence, different strategies have

been utilized in clinics, such as combining radiotherapy or chemotherapy to improve tumor antigenicity and immunoadjuvants to strengthen DCs function. The therapeutic outcomes have been enhanced to a certain extent but are far beyond the ideal state. In contrast, SDT may increase the response rate by providing abundant TAAs through massive ROS infiltration and exerting ICD to activate naïve DCs. Secondly, severe hypoxia and pathological lactic acid accumulation can affect tumor cellular energy metabolism, lead to excessive H_2O_2, aberrant angiogenesis, and effector T cell signaling suppression in direct and indirect ways. Normalizing tumor vessels and ameliorating hypoxia by combining anti-angiogenic drugs has improved ICI efficacy in clinical practice. In an open-label, phase 1 b study, 67 patients with unresectable hepatocellular carcinoma (HCC) were treated using pembrolizumab along with Lenvatinib and showed a high ORR of 44.8% [169]. Notably, severe adverse events occurred in 42 patients indicating that it is necessary to prevent the "off-target" effect [170]. Researchers have designed various low oxygen-sensitive nanomaterials, such as DDSs targeting the characteristic hypoxia of tumors. These versatile nanoplatforms can enhance the intracellular oxygen concentration in tumors in different ways and achieve controllable release by reducing the occurrence of adverse reactions [171]. For instance, Fu et al. fabricated a US-activatable nanomedicine that can overcome hypoxia-induced drug resistance and induce collaborative ferroptosis. The nanoplatform was designed by integrating Fe(VI) species and DOX into mesoporous silica and modified using temperature-sensitive *n*-heneicosane and PEG. Up on US-induced mild hyperthermia, Fe(VI) release could induce ferroptotic death through Fenton reactions and effectively react with the over-expressed H_2O_2 and GSH. Then, reoxygenation down-regulated the expression of hypoxia-inducible factor 1α and *P*-glycoprotein inside tumors [172].

4. Recent advances in NPs-based SDT/ICB synergistic therapy

A NPs-based SDT is one of the most promising tumor treatment modalities with clinical potential, particularly those resistant to current ICB therapies. This treatment can facilitate ICB therapy as follows: 1) SDT can induce ICD to provide abundant TAAs through ROS overproduction. 2) Versatile nanoplatforms can relieve hypoxia or deplete excessive H_2O_2 and GSH to produce oxygen. 3) Other apoptosis-related pathways, such as ferroptosis and autophagy, can be achieved by nanomaterials or loaded drugs. 4) High tumor-targeting capability, especially the control release switch, can enhance ICB and decrease adverse events [173,174]. Various preclinical studies combining NPs-based SDT with ICB have been conducted, with desirable therapeutic outcomes (Table 1). The most relevant SDT/ICB trials have been discussed as follows.

4.1. Organic sensitizers

The rapid collapse of micro-bubbles in the US can emit a small amount of optical energy. Since SL-based photochemical reaction is a pivotal mechanism in SDT, various organic semiconductors demonstrating good photocatalytic ability are gradually switched to sonosensitizers. Hence, optimizing photoconversion efficiency (i.e., energy band structure, absorption wavelength) and chemical properties (solubility) of traditional organic semiconductor photosensitizers can serve them well as sonosensitizers. Organic semiconductors have the advantage of a smooth, tunable structure with rich optical properties.

4.1.1. Porphyrin-derivatives

As the most ubiquitous organic dyes in nature, porphyrin and its derivatives, including hematoporphyrin, hematoporphyrin monomethyl ether (HMME), and verteporfin, have been extensively studied with critical roles in bioactive materials, particularly photo-/sonosensitizers [175–178]. The characteristic expanded π-aromatic structure of porphyrin-derivatives offers them relatively high efficiency in light absorption. However, they are easily aggregated in an aqueous environment due to the π−π interactions and their hydrophobic nature, leading to self-quenching in the excited state. Yue et al. designed an HMME-based nanosonosensitizers (HMME/R837@Lip) with high biocompatibility to improve the state such that all the components, including liposomes, co-encapsulated HMME, and immune adjuvants R837 become clinically approved [30]. As shown in Fig. 3A, a typical reverse evaporation method helped obtain the nanoplatforms. The as-prepared HMME/R837@Lip nanosonosensitizers dispersed in aqueous solutions exhibited a uniform quasi-spherical structure observed through TEM (Fig. 3B). An ESR assay helped analyze the corresponding ROS species to monitor the ROS-generating ability of HMME/R837@Lip, and a strong $^1O_2$ peak could be observed under US irradiation (Fig. 3C). Moreover, the DCs maturation caused by HMME/R837@Lip *in vivo* was also determined using flow cytometry. With son-irradiation, HMME/R837@Lip significantly enhances DCs maturation to facilitate cytokine secretion and adaptive immunity (Fig. 3D). Regarding $CD8^+$ cells, HMME/R837@Lip + US + PD-L1 group increased 2.7 times that of the control one, and the immunosuppressive Tregs also demonstrated a reduction pattern (Fig. 3E).

The high efficiency of the ROS-generating ability of porphyrin derivatives is beyond doubt. In contrast, the poor water solubility and potential toxicity of some porphyrin derivatives in early generations remain intractable. The HMME/R837@Lip fabricated by Yue et al. demonstrated prolonged blood circulation and a high bio-safety pattern by coating the drugs with liposomes. All FDA-approved components ensure minimal harmful effects on normal organs, providing new ideas for rapid clinical translation of the NPs.

Yang et al. developed 4-hydroxyphenyl-loaded fluorinated covalent conjugate polymers (PFCE@THPPpf-COPs) to relieve tumor hypoxia and reverse immunosuppressive TME [32]. PFCE@THPPpf-COPs plus anti-CD47 antibodies could cooperatively remove local tumors and metastases upon intratumoral injection. Moreover, a potent immune memory was elicited to prevent tumor rechallenge (Fig. 3F). The fluorinated THPPpf-COPs were prepared by the esterification reaction depicted in Fig. 3G. The molar ratio of THPP, PFSEA, and mPEG5k-COOH was 1: 1.5: 4. The perfluorocarbons (PFC) could induce tumor hypoxia attenuation. The TEM image indicated a typical spherical morphology of PFCE@THPPpf-COPs with a mean diameter of nearly 42 nm (Fig. 3H). Consistently, the CT26 cells incubated with THPPpf-COPs and PFCE@THPPpf-COPs under US irradiation depicted potent intracellular DCFH fluorescence, demonstrating the desirable ROS-generating capability of such sonosensitizer (Fig. 3I). Next, the anti-tumor efficiency of PFCE@THPPpf-COPs combining ICB therapy was also assessed using *in vivo* studies. Tumors were eliminated in four of the five mice within the combination treatment group (Fig. 3J). Furthermore, the effector memory T cell percentage from these cured mice was 23.1 ± 4.5%, significantly higher than healthy mice (17.2 ± 1.5%) (Fig. 3K). In addition, ELISA also depicts a high secretion level of TNF-α and IFN-γ among cured mice (Fig. 3L).

Jeon et al. demonstrated chemiluminescence resonance energy transfer (CRET)-based nanoparticles (iCRET) to elicit a synergistic sonoimmunotherapy [34]. The iCRET NPs could provide large ROS QY due to the high sensitivity to H_2O_2 in the TME upon son-irradiation and generate CO_2 bubbles causing necrosis and ICD by disintegrating the cancer cell membrane. The synthesis process is described in Fig. 3M. The PV NPs were self-assembled to the hydrophobic VPF core surface to form the core-shell structure. Then, an H_2O_2-responsive CRET donor dibutyl oxalate was encapsulated into cores of PV NPs as the energy donor and CO_2 generator to obtain the iCRET NPs (Fig. 3N). As shown in Fig. 3O, iCRET NPs demonstrated a spherical shape with size distribution of 132.53 ± 6.4 nm. The high-contrast harmonic images indicated that iCRET NPs generated massive CO_2 gas under H_2O_2-abundant conditions (Fig. 3P). With a combination of *anti*-PD-1 antibodies, the iCRET + US + aPD-1 treatment group (i-combi) completely inhibited tumor growth (Fig. 3Q). As for the anti-metastasis effect, the i-combi group

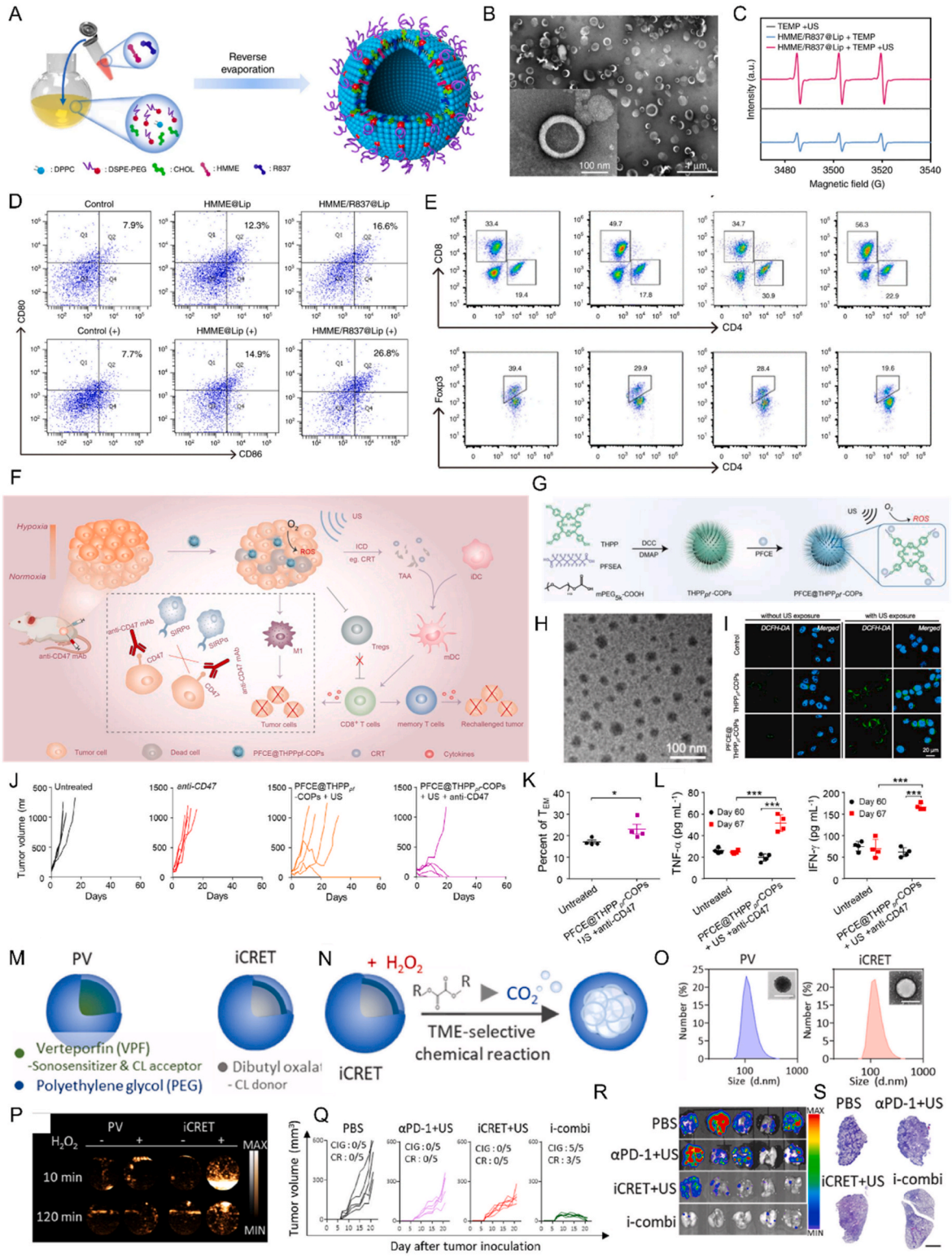

Fig. 3. (A) The schematic illustration of HMME/R837@Lip synthesis. (B) TEM image of HMME/R837@Lip. (C) The ESR spectra of HMME/R837@Lip with or without US. (D) The representative flow cytometry plots of DC maturation caused by HMME/R837@Lip in 4T1-bearing mice. (E) The representative flow cytometry plots of tumor-infiltrating $CD8^+$ T cells and $CD4^+$ T cells within distant tumors. Reproduced with permission from Ref. [30]. Copyright 2019, Springer Nature. (F) The schematic illustration of SDT combining ICB mediated by PFCE@THPPpf-COPs. (G) The schematic preparation of PFCE@THPPpf-COPs. (H) TEM image of PFCE@THPPpf-COPs. (I) The confocal microscopic image of ROS production of CT26 cells among different treatment groups with or without US. (J) The individual tumor growth curves after different treatments. (K) Flow cytometric analysis of TEM cell frequencies in blood obtained from each mouse before tumor inoculation at day 60. (L) The TNF-α and IFN-γ secretion levels in the sera were collected from each mouse at days 60 and 67. (M) The schematic illustration of PV NPs and iCRET NPs. Reproduced with permission from Ref. [32]. Copyright 2022, Elsevier. (N) The schematic illustration of CO_2 generation through CRET. (O) Size distribution and TEM image of PV and iCRET NPs. (P) *In vitro* US imaging of PV and iCRET NPs in the presence and absence of H_2O_2. (Q) The individual tumor growth curve for each group. (R) *Ex vivo* bioluminescence images of dissected lungs. (S) H&E-stained lung images. Reproduced with permission from Ref. [34]. Copyright 2022, Elsevier.

significantly suppressed lung metastasis compared to other treatment groups (Fig. 3R). The histological analysis shown in Fig. 3S also established the highest therapeutic efficacy of sonoimmunotherapy. The ROS QY also depends on oxygen supply. Simultaneously, the severe TME hypoxia caused by rapid tumor growth and abnormal blood vessel formation may impair the therapeutic effect of SDT. Moreover, tumors provide a high concentration of H_2O_2 enhancing tumor adhesion and regulating various signaling pathways associated with distant metastasis. Thus, alleviating hypoxia by antiangiogenesis or direct oxygen delivery via nanomaterials and consuming abundant H_2O_2 to oxygen has been a major concern in improving SDT. Yang et al. used PFC to enhance THPPpf-COPs-mediated SDT and efficiently induce ICD upon a low frequency of US being motivated by the oxygen loading capacity of PFC nanoshuttles using mesoporous structures. On the other side, Jeon et al. used the CRET response to H_2O_2 to develop a powerful oxygen source for ROS QY improvement. Reversing the hypoxia TME represents one of the most commonly used methods to enhance ROS QY. However, temporary oxygen delivery or persistent H_2O_2 consumption is not a permanent solution to abnormal blood vessels. Thus, anti-angiogenic drugs are encouraged to normalize tumor angiogenesis for a long-term oxygen supply and to relieve the acidic and immunosuppressive state of TME.

Chlorin e6 (Ce6) naturally degrades chlorophyll and has been extensively applied in PDT and SDT due to its high efficiency in developing $^1O_2$ [179–181]. The clear porphin structure leads to potent

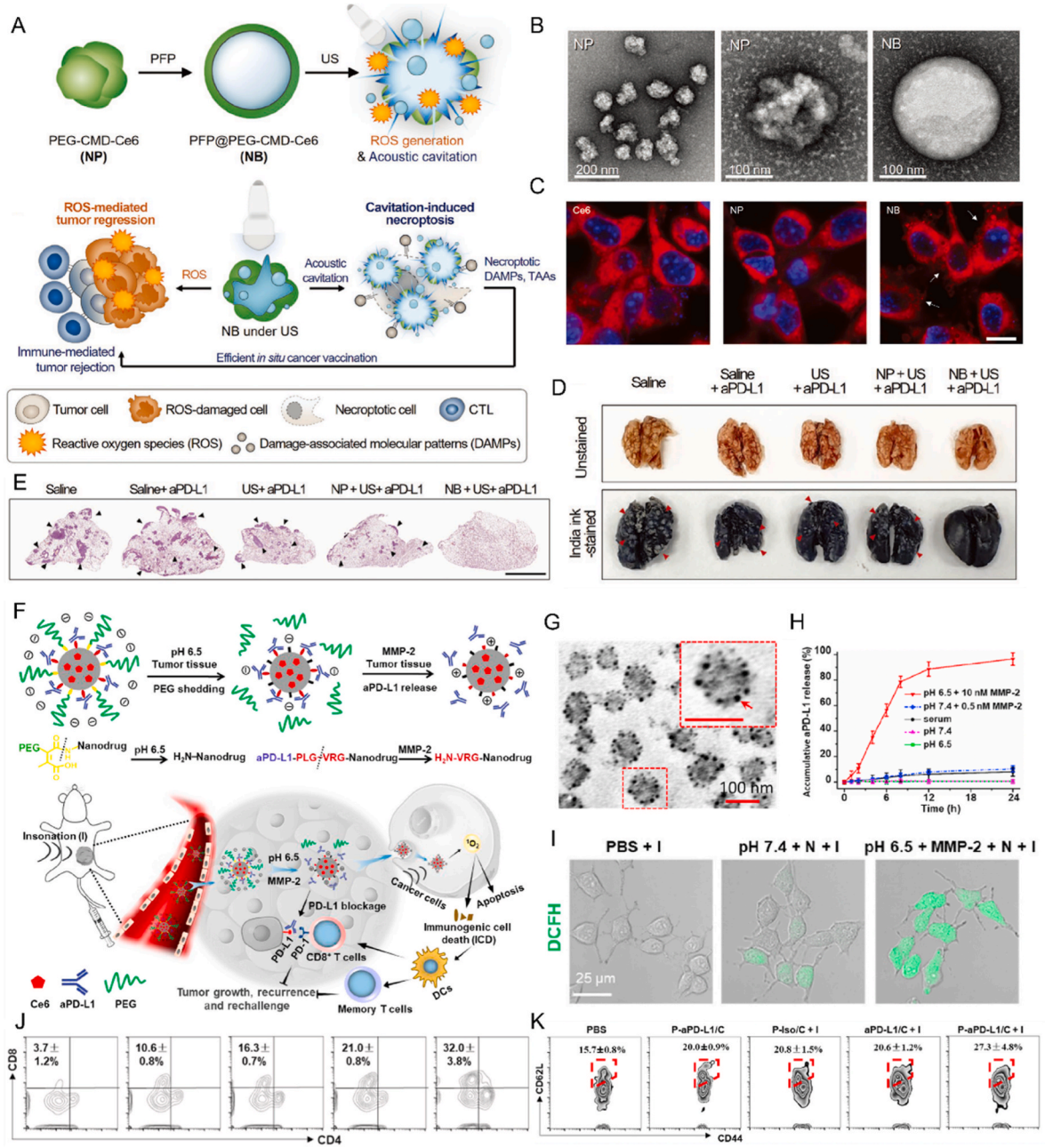

Fig. 4. (A) The schematic illustration of the intrinsic necroptosis-inducing mechanism using NBs. (B) The TEM images of NP and NB. (C) The confocal microscopy images of CT26 cells across various treatment groups. (D) India-ink staining lung tissues. (E) H&E-staining lung tissues. Reproduced with permission from Ref. [35]. Copyright 2020, John Wiley and Sons. (F) The schematic illustration of the tumor-targeting SDT-immunotherapy using dual-sensitive *P*-aPD-L1/C. (G) The TEM image of *P*-aPD-L1/C. (H) The *in vitro* releasing profile of aPD-L1 from nanodrugs based on different incubated conditions. (I) The analyses of intracellular ROS level. (J) The flow cytometry analysis of intratumoral $CD8^+$ T cell proportion. (K) The flow cytometry analysis of TCM proportion in blood on day 14 after the initial treatment. Reproduced with permission from Ref. [37]. Copyright 2021, Elsevier.

photo-sensitization in the ultraviolet–visible (UV–Vis) region and fast excretion than the early generation of photosensitizers. However, the hydrophobicity and easy aggregation of Ce6 limits lead to selective accumulation and bioavailability. Um et al. reported necroptosis-inducible nanobubbles (NBs) using perfluoropentane (PFP) as the gas precursor and Ce6 as the sonosensitizer to address these issues and improve therapeutic efficacy [35]. When exposed to US irradiation, these NBs could induce RIPK3-independent necroptosis through burst-mediated cell-membrane disintegration to activate adaptive immunity (Fig. 4A). The as-prepared NBs exhibited a smooth spherical shape. (Fig. 4B). Regarding cellular uptake, CT26 cell images under confocal microscopy depicted promising targeting behaviors of NPs and NBs (Fig. 4C). Notably, the lung tissues stained with H&E (Fig. 4D) and India ink (Fig. 4E) demonstrate that NB + US + aPD-L1 group significantly suppressed tumor metastasis. The NBs augment anti-tumor immunity by avoiding the RIPK3/MLKL signal pathway regulation by tumors and elicit a synergistic effect against tumors with PD-L1 checkpoint blockade. The exquisite design of such NBs was manifested. Firstly, the cell-membrane disintegration of tumors induced by physical force through gas blust generation reinforced the RS-regulated ICD. Secondly, the PEGylated carboxymethyl dextran provides hydrophilia to the nanoplatform to enhance blood circulation. Ultrasonic contrast agents are composed of inert perfluorocarbon gas combined with a polymer or protein. Still, the inert gas expands at body temperature and diffuses out of the loose shell, leading to a short half-life. Thus, applying NBs to ultrasound imaging and developing versatile NPs to integrate diagnosis and treatment simultaneously would be wonderful.

Huang et al. designed a unique lipid (LP)-based nanocarriers by encapsulating Ce6 as sonosensitizer, conjugating *anti*-PD-L1 antibodies (aPD-L1) to the interlayer through MMP-2-cleavable peptide, and bearing a low pH-responsive PEG coating to provide a dual sensitivity and synergistic anti-tumor effect (Fig. 4F) [37]. The structure of as-synthesized *P*-aPD-L1/C was observed, and the black dots indicate the decoration of aPD-L1 (Fig. 4G). Notably, the nanoparticles remained stable without MMP-2. In contrast, the release of antibodies could be effectively activated at pH 6.5 and 10 nM MMP-2 (Fig. 4H). Then, DCFH was utilized as a detection probe to determine the intracellular ROS level of different groups (Fig. 4I). The results indicated the highest green fluorescence intensity in the *P*-aPD-L1/C + pH 6.5 + 10 nM MMP-2 group, which showed a desirable sonoactivity of *P*-aPD-L1/C. Moreover, a remarkable elevation of infiltrating $CD8^+$ T cells was observed in *P*-aPD-L1/C + insonation treatment group (Fig. 4J). The data from flow cytometry revealed the highest amount of central memory T cells (TCM) within the *P*-aPD-L1/C + insonation group, indicating the potent immune memory developed by the synergistic strategy (Fig. 4K). Increasing biosafety or reducing adverse effects has a concern for medicine development. Huang et al. dexterously avoided the potential phototoxicity of Ce6 and "off-target" effects of aPD-L1 using a double insurance modification. The combination treatment theory would provide a better therapeutic outcome if the *P*-aPD-L1/C could co-load other agents while targeting different signal pathways.

4.1.2. Cyanine derivatives

As near-infrared dyes, the indole-derivative sensitizers, such as Indocyanine green (ICG), IR780, and IR820, have been widely recognized as outstanding phototherapeutic agents due to their excellent optical properties and high photoconversion efficiency [182–184]. Compared with early-generation UV–Vis dyes for PDT, these indole-derivative sensitizers provide better photo conversion upon NIR light activation. Moreover, they could serve as sonosensitizers upon US irradiation for SDT [185]. Tian et al. developed an IR780-based TME--sensitive phenolic nanoadjuvant (PIMS) encapsulating sabutoclax to decrease intracellular glutathione (GSH) levels [42]. The low pH-responsive phenolic polymer of the nanoadjuvants ensured Mn^{2+} integration and induced its sustained *in-situ* release in acidic TME to activate the cGAS-STING pathway. The PIMS NPs could mediate an effective DCs maturation with the ICD effect exerted by SDT. Moreover, the *anti*-PD-L1 injection could induce T-cell activation and elicit a potent anti-metastasis effect (Fig. 5A). The illustration of PIMS NPs synthesis is demonstrated in Fig. 5B. PIMS NPs exhibited an elliptic structure under TEM with approximately 70 nm in diameter (Fig. 5C). ICP-MS help investigate the releasing profile of Mn^{2+} from PIMS NPs in acidic conditions. The results revealed a much more rapid releasing curve in pH 6.8 compared to the physiological environment (Fig. 5D). Western blot analysis evaluated the cGAS-STING pathway activation. Moreover, PIMS NPs significantly activated the STING pathway and induced STING-dependent TBK1 and IRF3 phosphorylation (Fig. 5E). Thus, synergistic effects of Mn^{2+} and ICD in PIMS NPs result in the highest CD80 and CD86 expression level in DCs maturation (Fig. 5F). With a further combination of *anti*-PD-L1 antibodies, PIMS NPs induced a distinct upregulation in $CD8^+$ and memory T cells to inhibit lung metastasis and prevent tumor rechallenge (Fig. 5G and H). Regarding the adaptive immune response, the maturation and proliferation of DCs are directly associated with the subsequent activation and tumor-killing effect of a series of immune cells, including cytotoxic $CD8^+$ T cells. The release of Mn^{2+} into the cytoplasm can hyperactivate the cGAS-STING pathway, significantly enhancing the antigen-presenting ability of DCs. Studies have identified that GSH is crucial in regulating the REDOX balance in cells and is closely related to cancer development. In addition, high GSH levels in tumors can hinder various cancer treatment strategies, such as SDT. Tian et al. used PIMS to obtain the controllable release of Mn^{2+} and downregulate GSH levels to facilitate the SDT effect. The simultaneous enhancement of SDT and immune therapy could provide a significant outcome.

IR820 has been developed using better aqueous suspension ability and equal photosensitive ability to overcome the agglomeration and insolubility of ICG and IR780 [186]. Bai et al. reported a genetically engineered transferrin-expressing cell membrane nanovesicle (Tf@IR820-DHA) encapsulating IR820 as sonosensitizers to improve *anti*-PD-L1 blockade therapy [45]. Dihydroartemisinin (DHA) is a ROS-producing and ICD-inducing drug conjugated with IR820 through an acid-responsive ester bond linker to develop an amphiphilic prodrug. The Tf@IR820-DHA NPs demonstrated an excellent tumor-targeting effect and induced Fe(III)-mediated programmable catalysis of DHA and glutathione (GSH) depletion to synthesize many ROS. Moreover, the DHA could decrease the activation of immunosuppressive Tregs, thereby remodeling the "cold" TME. The preparation and formation of Tf@IR820-DHA NPs are illustrated in Fig. 5I. The co-expressed green fluorescent protein (GFP) signals indicated the successful transferrin anchor onto the cell membrane (Fig. 5J). The Tf@IR820-DHA NV morphology was depicted using TEM (Fig. 5K). The fast releasing rate of Tf@IR820-DHA NVs at low pH values indicated the acidic responsive hydrolyzed property, indicating its excellent biocompatibility and stability (Fig. 5L). The H&E, TUNEL, and Ki67 staining of the distal tumors anchored in the Tf@IR820-DHA NVs group exhibited severe damage. Additionally, the significant upregulation of $CD4^+$ T cells, $CD8^+$ T cells, and the cytokine levels with immunosuppressive $Foxp3^+$ Tregs inhibition established the potent adaptive immune response caused by Tf@IR820-DHA NVs-mediated combined with sonodynamic-immunotherapy (Fig. 5M). In this trial, applying ICD-inducing DHA and Fe(III)-mediated glutathione (GSH) depletion significantly enhances the practical effect of SDT. The activated DHA can downregulate the level of Tregs during anti-tumor immunity, thereby proliferating and maturing other immunostimulatory cells.

4.1.3. Semiconducting polymer

Semiconducting polymer NPs (SPNs) are attractive agents for PTT, PDT, or SDT due to their excellent optical properties, different from the traditional organic sensitizers with poor photostability. This included a significant absorption coefficient in the near-infrared region, high photostability, easy surface modification, adjustable size, and simple preparation processes [187,188]. Particularly, SPNs indicate a

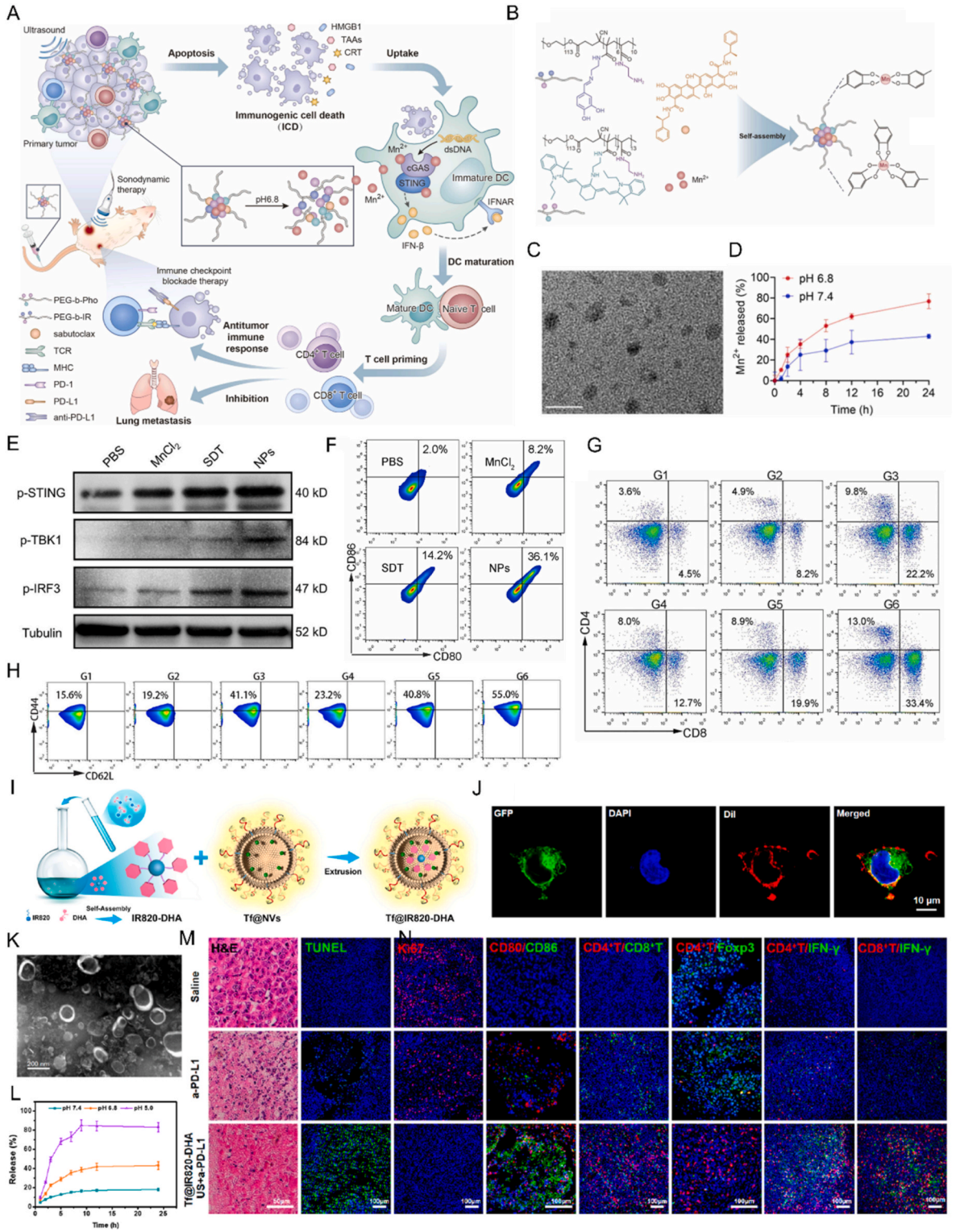

Fig. 5. (A) The schematic illustration of phenolic nanoadjuvant enhances significant maturation of dendritic cells and sensitizes tumors to PD-L1 checkpoint blockade immunotherapy. (B) The scheme indicates the self-assembly preparation of PIMS NPs and chemical structures (PEG-b-Pho, PEG-b-IR, and sabutoclax). (C) TEM images of PIMS NPs. (D) The percentages of released Mn^{2+} from PIMS NPs over time between the pH 6.8 and 7.4 buffer. (E) After different treatments with PBS, $MnCl_2$, SDT, or PIMS NPs, 4T1 cells were incubated using BMDCs and followed by analyzing the cGAS STING pathway activation using western blot analysis. (F) Flow cytometric analyses of mature DCs ($CD80^+$ $CD86^+$ gated on $CD11c^+$). (G) Flow cytometric analyses of $CD4^+$ T and $CD8^+$ T cells within distant tumors. Reproduced with permission from Ref. [42]. Copyright 2022, Elsevier. (H) Flow cytometric analyses of memory T cells ($CD3^+$, $CD8^+$, CD44high, CD62Llow) inside the splenocytes. (I) A schematic illustration of the self-assembly of IR820-DHA NPs and Tf@IR820-DHA NV formation. (J) Verification of Tf expression. (K) The morphological images of Tf@IR820-DHA NVs. (L) DHA release of Tf@IR820-DHA NVs based on different treatments. (M) H&E, TUNEL, Ki67, CD80/CD86, $CD4^+$ T/$CD8^+$ T and $CD4^+$ T/$Foxp3^+$, $CD4^+$ T/IFN-γ, and $CD8^+$ T/IFN-γ tumor staining using different treatments. Reproduced with permission from Ref. [45]. Copyright 2022, American Chemical Society.

promising prospect in biomedicines due to the inexistence of toxic metal ions. In contrast, the limited penetration depths of light impose application-related restrictions [189]. Zeng et al. reported a US-triggered semiconducting polymer-based sensitizer (SPN_{Ab}) to exert an activatable sonodynamic-immunotherapy [46]. SPN_{Ab} primarily comprises three components: the backbone of semiconducting polymer and PEG chains, $^1O_2$-cleavable linker, and *anti*-CTLA4 antibodies (Fig. 6A). The *anti*-CTLA4 antibodies on SPN_{Ab} exhibit relatively low binding activities until a son-irradiation is provided under physiological conditions. The generated $^1O_2$ induces ICD in tumors to promote adaptive immunity and cleaves the $^1O_2$-cleavable linkers to unleash *anti*-CTLA4 antibodies and trigger checkpoint blockades *in situ*. SPN_{Ab} was studied and compared with the control nanoparticles SPN_C, which was developed by conjugating PFODBT-N_3 with mPEG-alkyne. As shown in Fig. 6B, both SPN_{Ab} and SPN_C exhibited a spherical structure. The electron paramagnetic resonance (ESR) spectra of SPNs demonstrated evident characteristic peaks of $^1O_2$ and hydroxyl radicals (•OH) upon US irradiation, confirming the dominant ROS species (Fig. 6C and D). The $^1O_2$ generation capability of SPN_{Ab} and SPN_C was also investigated, and FDA-approved sonosensitizer indocyanine green (ICG) and methylene blue (MB) were utilized as comparisons. The increasing brightness of $^1O_2$ sensor green (SOSG) in the SPN_{Ab} group shown in Fig. 6E was much higher than other sensitizers, depicting that SPN_{Ab} could serve as good sonosensitizers. Then, the CTLA-4 releasing efficacy of SPN_{Ab} was assessed using the US, possessing a high percentage of 96.7% after four irradiation cycles (Fig. 6F). The intracellular generation of $^1O_2$ in 4T1 cells was also studied using SPN_{Ab} and SPN_C. The strong fluorescence signals established the desirable ROS generation capability of SPNs (Fig. 6G). The synergistic son-immunotherapy elicited by SPN_{Ab} was assessed in the 4T1 model. The H&E staining images depict that SPN_{Ab} eradicated lung metastasis under son-irradiation, suggesting a significant anti-metastasis therapeutic effect (Fig. 6H). Furthermore, SPN_{Ab} caused a durable immunological memory by enhancing the expression level of $CD8^+$ effector memory T cells ($CD44^+$ $CD62L^-$) within the lymph nodes to prevent tumor rechallenge (Fig. 6I).

According to the same principles, Li et al. fabricated a semiconducting polymer immunomodulatory nanoparticles (SPINs) using two immunomodulators (NLG919 & *anti*-PD-L1 antibodies) conjugated by $^1O_2$-cleavable linkers to apply a US-activatable sonodynamic-immunotherapy (Fig. 6J) [47]. The chemical structure of SPN7 is depicted in Fig. 6K. The synthesis process of SPNs using nanoprecipitation is illustrated in Fig. 6L. The as-prepared SPN7 exhibited a uniform spherical morphology and provided the highest $^1O_2$ yield (34.5 nmol/μg) compared with other SPNs (Fig. 6M and N). Furthermore, the sonodynamic SPN7 properties were investigated competently with other sensitizers such as ICG, protoporphyrin IX (PpIX), acridine orange (AO), and inorganic TiO_2 NPs. The results indicated that SPN7 exhibited remarkable efficiency with high stability after four US irradiation cycles (Fig. 6O and P). The above data showed that SPN7 was an optimal sonosensitizer for SDT applications. The schematic illustration for SPIN synthesis is described in Fig. 6Q, and the molar ratios of NLG919/aPD-L1 modification in SPINs are demonstrated in Fig. 6R. The release profiles of aPD-L1 and NLG919 in $SPIN_{D2}$ solution were investigated with 10-cm pork tissue coverage under US irradiation. Fig. 6S shows that the releasing profile of aPD-L1 and NLG919 from $SPIN_{D2}$ did not exhibit apparent differences with or without 10 cm tissue coverage. Therefore, the profile depicted the desirable deep-tissue sonodynamic activation of $SPIN_{D2}$. Regarding the *in vivo* therapeutic effect, $SPIN_{D2}$ significantly suppressed the tumor growth locally and distantly in Panc02 tumor-bearing mice (Fig. 6T).

The above two experiments revealed that semiconducting polymer NPs could exhibit uniform sphere microstructures and have a stronger ability to produce $^1O_2$ than some commercial FDA-approved sonosensitizers. The conjugation of $^1O_2$-cleavable linkers prevents the dispensible activation of ICIs using NP insurance. This simultaneously enhances adaptive immune response and reduces the occurrence of adverse effects. Primarily, $SPIN_{D2}$ represented a prominent activation upon US irradiation in mice even when covered with 5 cm pork tissue indicating that SDT could provide better efficacy in targeting deep-seated tumors than PDT. The semiconducting polymer NPs-mediated SDT significantly enhanced ICIs by regulating ICD to exert immune response and a potent anti-metastasis ability was observed in both trials. It would be better to establish re-challenge models to validate the existence of prolonged immune memory.

4.1.4. Methylene blue (MB)

Recently, the utilization of Methylene blue (MB), a promising photosensitizer, has received attention [190]. MB is an FDA-approved agent offering high singlet oxygen QY under light irradiation along with fair and desirable water solubility [191]. Based on the similarity of SDT and PDT, MB can also be utilized as sonosensitizers to regulate ROS production [192]. Lei et al. prepared a GSH-activable platform (MRP NPs) combining Leu-MB with R837 to exert a joint SDT/ICB therapy (Fig. 7A) [48]. The microstructure of MRP NPs incubated with GSH or not is depicted in Fig. 7B. The disintegration of MRP NPs into nanodots demonstrated excellent GSH sensitivity. Moreover, ESR spectroscopy was used to illustrate the sonoactivity of MRP NPs. The results validated a characteristic peak of $^1O_2$ in the pretreated MRP + US group (Fig. 7C). Moreover, PD-L1 expression of tumors after MRP NPs + US treatment was assessed to determine the effect of such immunosonodynamic therapy. The results depicted a significant PD-L1 upregulation, hampering the sequential treatment (Fig. 7D). Therefore, *anti*-PD-L1 antibodies helped achieve an optimized therapeutic effect. The incremental proportion of $CD80^+$ $CD86^+$ DCs demonstrated an elevated maturation by MRP NPs (Fig. 7E). MRP + US + α-PD-L1 depicted a significant increase in infiltrating $CD8^+$ T cells with a further combination of ICB therapy (Fig. 7F). This trial used GSH-sensitive disulfide bonds to link the reduced MB and toll-like receptor 7 agonist R837 while achieving a TME-responsive profile. The *in-situ* MB release could mediate SDT under US irradiation and prevent phototoxicity, while R837 could stimulate DC maturation. GSH level depletion could enhance ROS production. This strategy strengthens the preponderance of SDT + ICB and covers the shortage by using R837 for α-PD-L1 and consuming GSH with SDT.

4.2. Inorganic sensitizers

Compared to organic semiconductors, the inorganic ones have the following advantages: 1) More nucleation sites are provided to improve the cavitation effect and ROS production. 2) Favorable physiochemical properties lead to a stable sonodynamic effect. 3) Surface modification provides possible functions, such as improved targeting ability or enhanced blood circulation. 4) Less phototoxicity and drug-related immunogenicity. This study describes some representative instances of inorganic sonosensitizers-induced SDT/ICB synergistic therapies.

4.2.1. TiO_2 NPs

TiO_2 NPs, as the most representative inorganic sonosensitizer, have been widely used in SDT because of their excellent chemical stability and low phototoxicity [193–195]. Compared with most organic sonosensitizers, the long-term stability under physiological conditions renders TiO_2 a better biosafety profile. Tan et al. designed a transformable nanosensitizer by coating an acidic degradable CaP shell onto a TiO_2 core to achieve controlled release and improve tumor agent aggregation [50]. Upon acidic TME exposure, the fabricated TiO_2@CaP can disintegrate into TiO_2 and Ca^{2+} as a controllable switch for ROS generation, thereby preventing off-target toxicity. The overloading of Ca^{2+} can amplify ICD for cytotoxic T-cell infiltration. Combined with aPD-1, TiO_2@CaP could eradicate the primary tumors and suppress lung metastasis (Fig. 8A). As shown in Fig. 8B, a thermal decomposition method helped in TiO_2 NPs synthesis. A CaP shell was coated on the surface to develop TiO_2@CaP. The TEM image indicated a clear

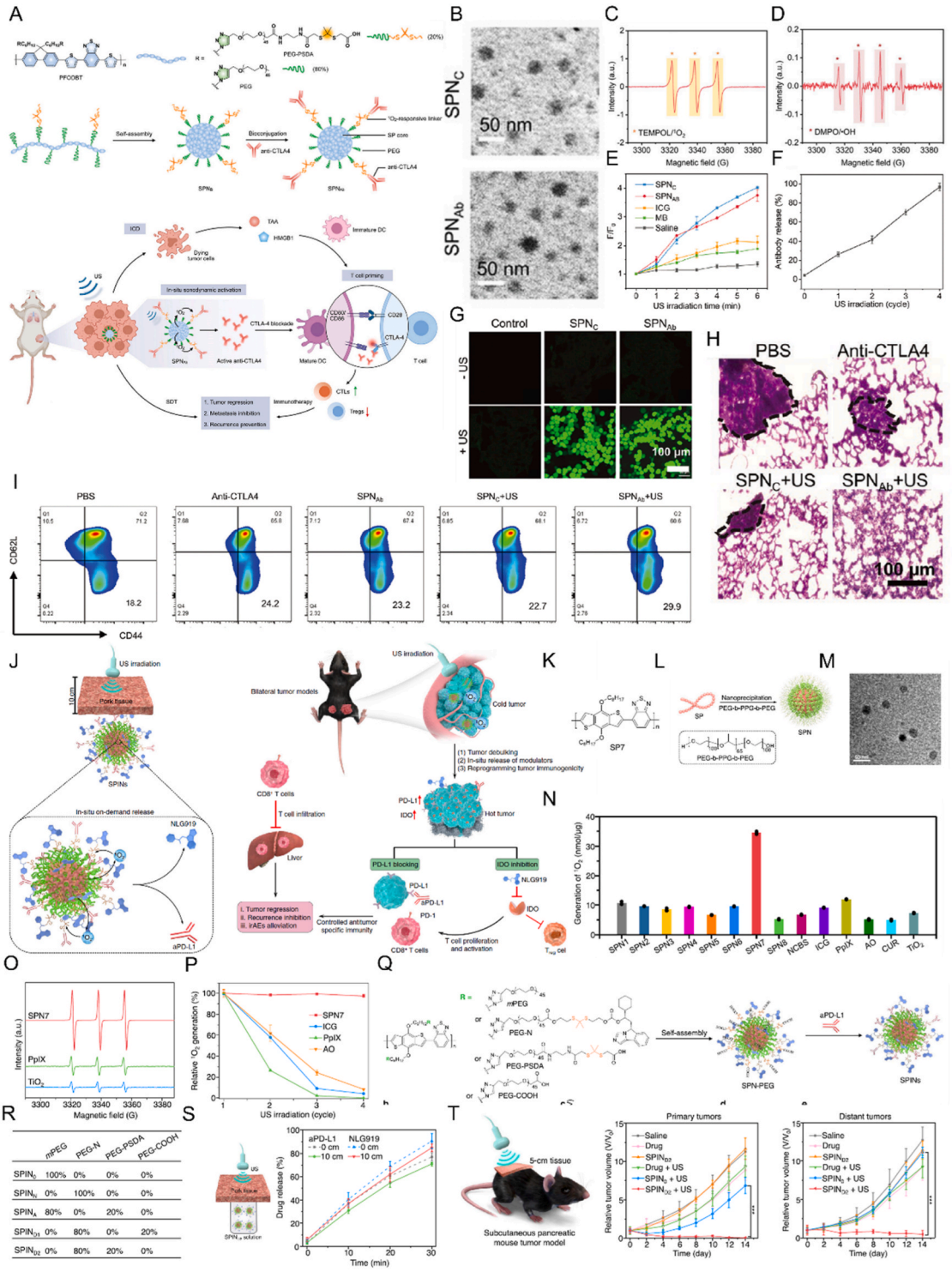

Fig. 6. (A) The schematic of preparation steps of SPN_{Ab} and SPN_{Ab}-mediated activatable son-immunotherapy. (B) The representative TEM images of SPN_C and SPN_{Ab}. (C) $^1O_2$ detection demonstration using the ESR spectra under US. (D) •OH detection demonstration using the ESR spectra under US. (E) Fluorescence improvement of SOSG for SPN_C, SPN_{Ab}, ICG, MB, and saline under US. (F) The releasing profile of *anti*-CTLA4 antibody from SPN_{Ab} with enhancing US irradiation time. (G) The representative confocal images of intracellular $^1O_2$ generation in 4T1 cells post-treatment. (H) H&E staining of lung metastases. (I) The representative flow cytometry plots depicting $CD8^+$ effector memory T cells in the lymph nodes of mice surviving for 21 days after different treatments. Reproduced with permission from Ref. [46]. Copyright 2022 John Wiley and Sons. (J) The schematic illustration of activatable deep-tissue sonoimmunotherapy using SPINs. (K) SP7 chemical structure. (L) The synthesis of SPNs using nano-precipitation. (M) TEM image of SPN7. (N) The quantification of $^1O_2$ generation among different samples. (O) The ESR spectra of SPN7, PpIX, and TiO_2 NPs using US irradiation. (P) The relative $^1O_2$ generation for SPN7, ICG, PpIX, and AO after different US irradiation cycles. (Q) The chemical structure and surface modification of amphiphilic semiconducting polymeric modulators to form SPINs. (R) The molar ratios of each component across different SPINs. (S) The schematic illustration of US irradiation of $SPIN_{D2}$ solutions covered using pork tissue and ESR spectra of $^1O_2$ for $SPIN_{D2}$ post-US irradiation with or without pork tissue coverage under different thicknesses. (T) The schematic of son-immunotherapy of subcutaneous pancreatic mouse tumors was covered using 5 cm tissue. After various treatments, the relative tumor volumes of primary and distant Panc02 tumor-bearing C57BL/6 mice could be observed (n = 5). Reproduced with permission from Ref. [47]. Copyright 2022 Springer Nature.

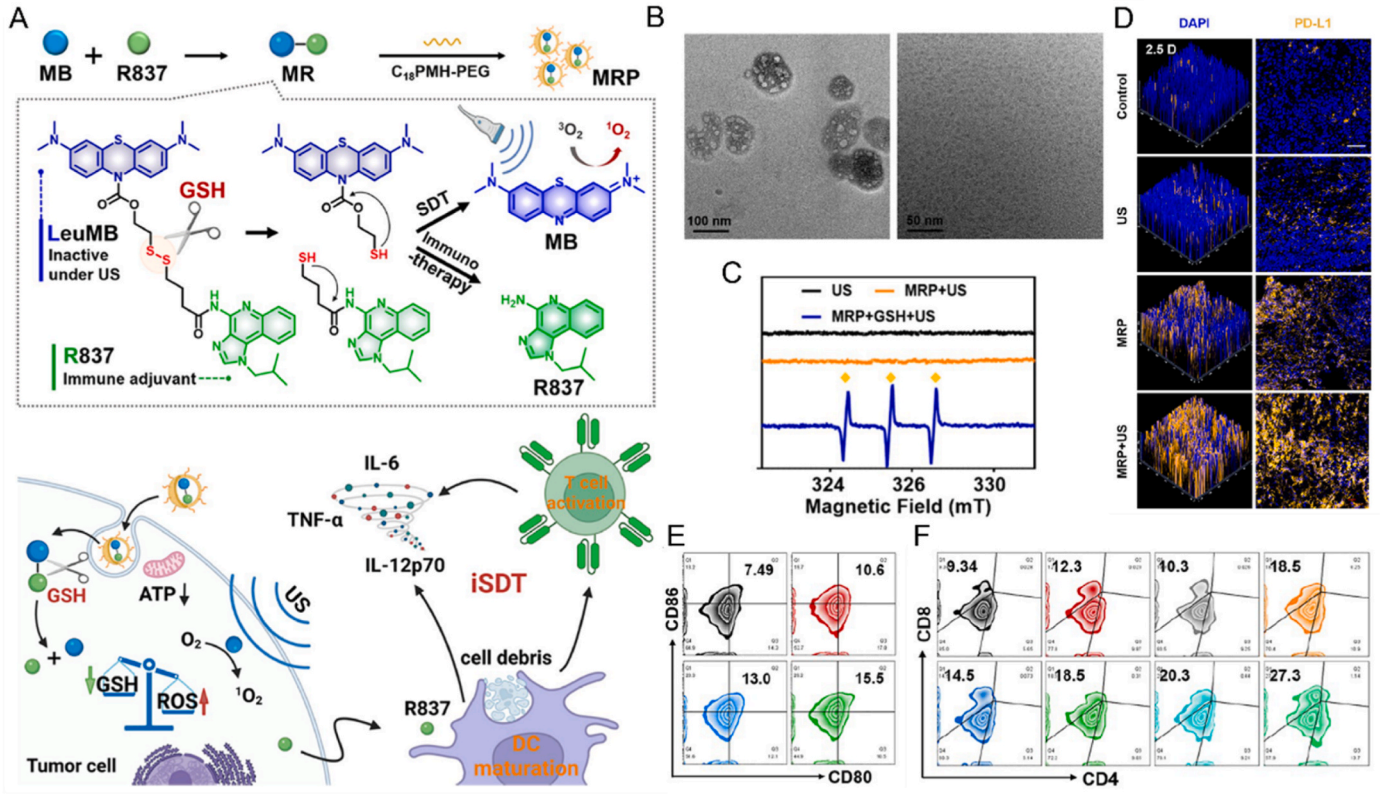

Fig. 7. (A) The schematic representation of MB-R837-PEG (MRP) nanoparticles for GSH-activated immunosonodynamic therapy (iSDT). (B) The TEM images of MRP NPs before (a) and after (b) GSH incubation. (C) The ESR spectra of TEMP/$^1O_2$ adducts across different solutions under US irradiation. (D) The immunofluorescence staining of PD-L1 expression in the tumor sections on day 5, after two treatment cycles. (E) The representative flow cytometric analysis of DC maturation ($CD80^+$ $CD86^+$) in the lymph nodes, gating on $CD11c^+$ cells. (F) $CD8^+$ T cells in $CD3^+$ T cells within primary and distant tumors. Reproduced with permission from Ref. [48]. Copyright 2022, American Chemical Society.

spherical core-shell structure of TiO_2@CaP (Fig. 8C). Regarding the sonodynamic capability, a fluorescent ROS indicator DCFH-DA and Ca^{2+} detector Fluo-4AM facilitated confocal laser scanning microscopy imaging. Compared with the neutral condition, we could observe a higher fluorescence of free Ca^{2+} in the acidic environment, indicating the desirable pH-response ability of TiO_2@CaP (Fig. 8D). Moreover, the ROS generation capability of TiO2@CaP was synergistically improved by releasing Ca^{2+} at lower pH values (Fig. 8E). Next, DAMP levels in the TiO_2@CaP + US group, including ATP, were 5.8 fold to the control group (Fig. 8E). The results demonstrated that TiO_2@CaP elicited a powerful ICD effect to boost the anti-tumor immune response, facilitating ICB therapy. The TiO_2@CaP + aPD-1 group exhibited the most distinct metastasis inhibition by relieving immunosuppression with the combination of *anti*-PD-1 antibodies (Fig. 8F). The inception of an acidic TME-responsive transformable nanoplatform of "no effect in normal tissues, but toxic in tumors" has become more attractive due to high targeting and low adverse effect. The release of abundant Ca^{2+} could further amplify ICD and facilitate the aPD-1 functions.

Wei et al. reported a dual-targeted TiO_2-based nanosensitizer by functionalizing the surface using the melanoma cell membrane and an *anti*-PD-L1 antibody to improve the active-targeting ability and overcome the poor bioavailability of sonocatalytic nanoagents (SCN) (Fig. 8H) [51]. The as-prepared SCN@B16F10 M/PEG-aPD-L1 NPs exhibited an irregular nanosphere structure. Moreover, the yellow arrows indicated a successful cell membrane coating (Fig. 8I). Upon deep-penetrating via US irradiation, SCN@B16F10 M/PEG-aPD-L1 revealed a much higher ROS production than the single-targeting strategy group (Fig. 8J). The confocal laser scanning microscopy (CLSM) images also demonstrated an excellent homology and PD-L1-specific dual-targeted ability of such cell-mimetic functionalized SCNs (Fig. 8K). Additionally, the high ROS concentration achieved by the dual-targeting nanoplatform could activate effector $CD8^+$ T cells and simultaneously enhance the immunotherapeutic effect of the *anti*-PD-L1 antibody. For this trial, the innovative point is coating the melanoma cell membrane and modifying aPD-L1 to ensure the dual active targeting effect and better TiO_2 biocompatibility. The significantly improved targeting ability elevated the ROS level in tumors and guaranteed better biosafety.

The low ROS-generating efficiency of TiO_2 NPs is a significant drawback. Compared to the unsatisfactory ROS QY of traditional white TiO_2, the reduced black TiO_2 possesses abundant oxygen defects (O_v), facilitating e^- and h^+ separation to improve $^1O_2$ production [196]. Additionally, high NO concentration in tumors can induce mitochondrial dysfunction and DNA double-strand breaks to enhance apoptosis [197]. Thus, Wang et al. fabricated a black mesoporous TiO_2 (BMT)-mediated multifunctional nanovaccine loaded with L-arginine (LA) for improved sonodynamic/NO-gas therapy [52]. The US can simultaneously trigger BMT and LA to form ROS and NO gas in tumor regions. Intriguingly, $^1O_2$ can improve LA oxidation for extra NO production, synergistically inducing tumor apoptosis (Fig. 8L). The TEM image depicted a uniform mesoporous spherical structure of BMT (Fig. 8M). Compared to the 54.7% of the traditional mesoporous TiO_2 (MT) group, the 1′3-diphenylisobenzofuran concentration of the BMT group decreased by 25.5% at 9 min. This indicated a better $^1O_2$-generating ability of BMT (Fig. 8N). As for NO production, the BMT@LA group depicted the most significant increase (approximately 238.4%) in intracellular NO levels. The lower NO production of BMT@LA + NaN_3 (used as a $^1O_2$ quencher) group confirms the previous theory of $^1O_2$-mediated NO level promotion (Fig. 8O). The *in vitro* studies indicated the potent $^1O_2$/NO generation and tumor-killing ability of

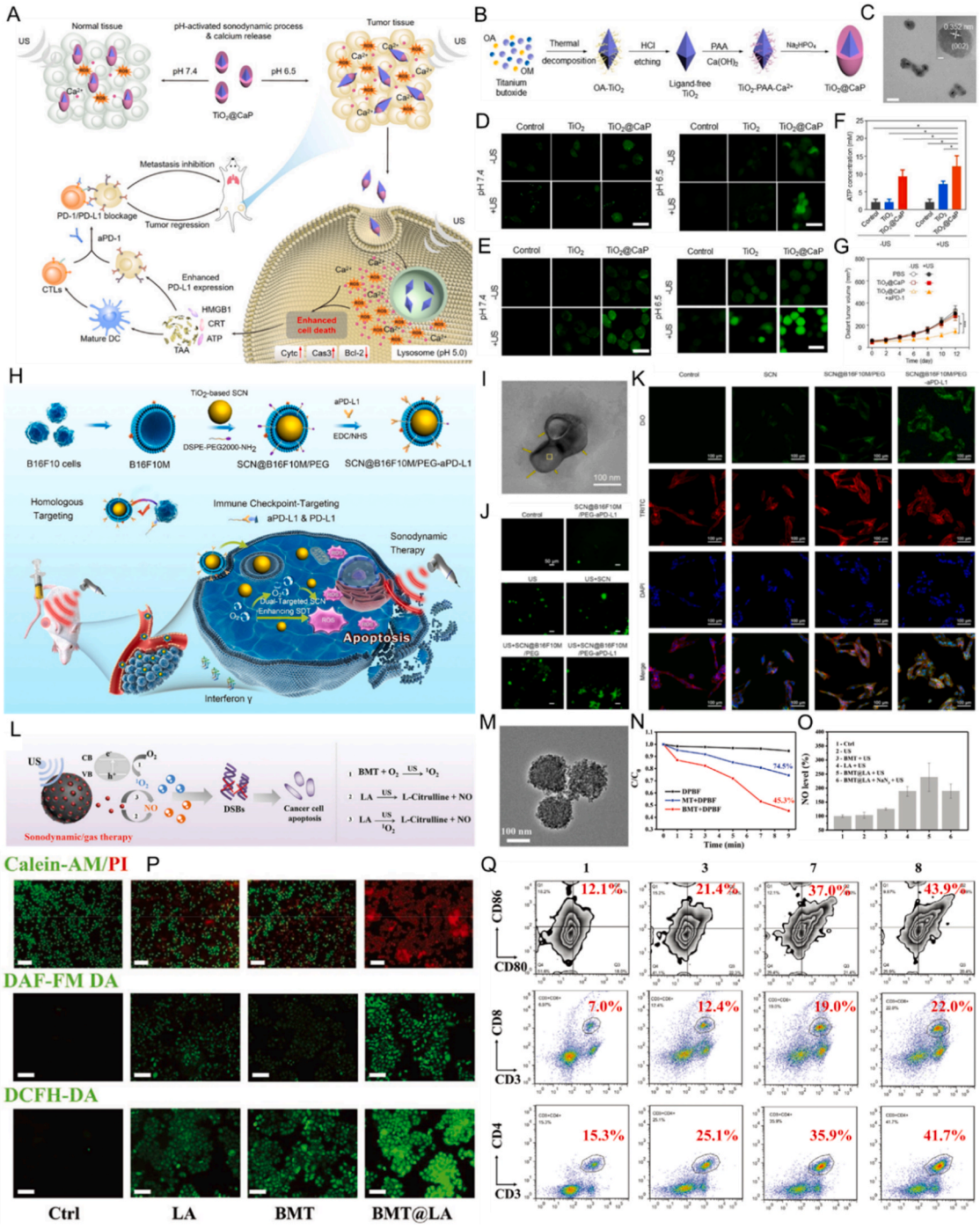

Fig. 8. (A) The schematic illustration of transformable TiO2@CaP in physiologically neutral and pathologically acidic conditions. The detailed mechanism to boost son-immune therapeutic efficacy in tumors has been depicted. (B) The diagram shows the synthesis of TiO2@CaP nanoparticles, oleic acid (OA), and oleylamine (OM). (C) The TEM images of TiO2@CaP NPs. (D) The confocal fluorescence images of Ca^{2+} in 4T1 cells incubated using TiO_2 and TiO_2@CaP NPs overnight in FBS free culture medium at pH 7.4 or 6.5 after US activation for 10 min. (E) The confocal fluorescence images of ROS in 4T1 cells incubated using TiO_2 and TiO_2@CaP NPs overnight in FBS free culture medium at pH 7.4 or 6.5 after US irradiation for 10 min. (F) ATP release from 4T1 cells incubated using TiO_2 or TiO_2@CaP after US activation for 10 min. (G) The growth curves of distant tumors in 4T1 tumor-bearing mice post various treatments. Reproduced with permission from Ref. [50]. Copyright 2021 John Wiley and Sons. (H) The schematic illustration of homology and immune checkpoint dual-targeted and enhanced SDT of tumors using SCN@B16F10 M/PEG-aPD-L1. (I) The TEM images of SCN@B16F10 M/PEG-aPD-L1. (J) The fluorescence microscopy images of ROS generation within melanoma cells. (K) The CLSM images of cell-mimetic functionalized SCNs through DiO staining B16F10 M under 200 ng/mL of IFN-γ. Reproduced with permission from Ref. [51]. Copyright 2021, American Chemical Society. (L) The schematic illustration of *in vitro* synergistic sonodynamic/gas therapy. (M) The TEM images of BMT. (N) DPBF absorption at 420 nm during DPBF, MT + DPBF, and BMT + DPBF group decomposition. (O) NO level of HeLa cells treated with different materials. (P) Calcein-AM&PI dual staining to identify the live or dead cells, DAF-FM DA probe to detect NO generation, and DCFH-DA probe to determine the OS level. (Q) The flow cytometric analyses of the mature DC cell populations ($CD11^+$ $CD80^+$ $CD86^+$ as the marker), $CD8^+$ ($CD3^+$ $CD8^+$ as the marker) T cells, and $CD4^+$ ($CD3^+$ $CD4^+$ as the marker) T cells within the spleen among different groups. Reproduced with permission from Ref. [52]. Copyright 2021 John Wiley and Sons.

BMT@LA upon US irradiation (Fig. 8P). As for *in vivo* assessment, BMT@LA exhibited the best tumor inhibition and exerted a prolonged immune activation to enhance ICB therapy. Around 43.9% of DCs in the spleen matured after BMT@LA + US+αPD-L1 treatment. Moreover, the T-cell activation level is nearly three times that of the control groups (Fig. 8Q). BMT@LA, designed by Wang et al. used reduced black mesoporous TiO_2 as a sonosensitizer and drug-delivery platform. The black TiO_2 indicated a better $^1O_2$ generating ability, and the loaded LA helped improve ICD using NO therapy. Based on the above two trials regarding TiO_2, aGSH-responsive membrane coating would improve SDT and enable controllable drug release.

4.2.2. Inorganic composite sensitizers

Among many methods to enhance SDT efficacy, the construction of inorganic composite sensitizers has been a representative due to enhanced ROS production or potential assistance by other bioactivities, including Fenton-like reaction. Zhang et al. synthesized AuNPs on the surface of black phosphorus quantum dots-doped mesoporous silica frameworks (Au-BMSNs) *in situ* to improve their sonodynamic performance and fabricate a desirable SDT agent with strong and stable ROS generation capability. CO-releasing molecules CORM-401 were loaded into Au-BMSNs to stimulate a combined therapy. The exogenous macrophage membrane was decorated to bypass the reticuloendothelial system clearance and enhance tumor-targeting ability [54]. IDO inhibitor NLG919 was applied to develop the triple synergistic treatment strategy and inhibit lung metastasis and tumor rechallenge (Fig. 9A). The as-synthesized N@CAu-BMSNs demonstrated a typical spherical morphology of 49.5 ± 5.6 nm with successful AuNPs decoration (Fig. 9B). The time-dependent reduction of DPBF absorbance suggested a desirable ROS-generating ability of Au-BMSNs (Fig. 9C). Notably, the $^1O_2$ generation triggered by US irradiation improved the oxidant sensitivity of CORM-401 to release extra CO gas (Fig. 9D). The representative photos and H&E staining images of excised lungs describing the *in vivo* therapeutic effect established that N@CAu-BMSNs combining NLG919 more significantly inhibited 4T1 distal metastasis than other monotherapies (Fig. 9E and F). NLG919 could potentially increase the antigen-presenting ability of APCs and block IDO-induced Tregs activation. Therefore, the DCs maturation and Tregs population in the primary tumor was analyzed using FACS (Fig. 9G and H). We observed a distinct DCs activation and a prominent Tregs inhibition in the combination treatment group. The results confirm the promising therapeutic effect of the SDT/CO/IDOi triple treatment strategy. This trial applied the macrophage membrane and mesoporous silica to ensure the high biocompatibility of N@CAu-BMSNs. The doping of AuNPs and BPQDs functions as a suitable sonosensitizer. The CO therapy controlled by CORM-401 could be strengthened using the $^1O_2$ generation. Together with NLG919, the N@CAu-BMSNs exert a dual improvement of anti-tumor immune response.

$CoFe_2O_4$ is a superior nanocatalyst and has been widely investigated in the bio-energy and environmental fields [198]. Fu et al. designed PEGylated $CoFe_2O_4$ nanoflowers (CFP) using various enzymatic abilities to provide synergistic SDT and CDT combinations for tumor treatment [55]. The CFPs are a brand-new sonosensitizer with strong Fenton-like and catalase-like activity for H_2O_2 decomposition because of the intrinsic Co^{2+}/Co^{3+} and Fe^{2+}/Fe^{3+} redox couples (Fig. 9I). A well-defined flower-like structure is represented in the TEM image of CFP (Fig. 9J). The selected area electron diffraction pattern of CFP demonstrated a body-centered cubic crystal structure (Fig. 9K). The cell apoptotic level was determined by assessing the expression of apoptosis-related biomarkers, such as poly (ADP-ribose) polymerase (PARP) and pro-caspase 3, significantly elevated in the CFP + H_2O_2 + US group (Fig. 9L). Additionally, the down-regulated expression of metastasis-related protein VEGF and MMP-9 and the accumulation of *E*-cadherin in 4T1 cells describes the significant anti-metastatic ability of CFP + H_2O_2 + US (Fig. 9M). The *in vitro* cytotoxicity studies also demonstrated the most outstanding tumor-killing effect, ROS QY, and tumor cell membrane disintegrating ability of the CFP + H_2O_2 + US group (Fig. 9N). The CFP + US + aPD-L1 group significantly decreased lung metastatic nodules by robustly activating anti-tumor immunity (Fig. 4O). The dual SDT/CDT function of CFP could benefit by depleting the H_2O_2 in TME. The high *E*-cadherin expression established that this strategy induced a potent ICD. With the further injection of aPD-L1, a long-term immune memory was formulated against tumor metastasis and rechallenge.

4.2.3. MOF

Nano-size metal-organic frameworks (nMOFs) are hybrid-based metal ions or clusters-based crystalline porous polymers formed by organic ligand coordination [199]. MOFs have multiple characteristics, such as highly specific surface area, tunable pore size, and ample inner space for nanodrug delivery [200]. Meanwhile, the easily modified chemical properties of MOFs have various biological applications [201]. As for SDT, Porphyrin-based nMOFs with favorable optoelectronic properties have demonstrated promising ROS-producing efficiency, rendering them reliable sonosensitizers [202]. Thus, Luo et al. developed a triphenylphosphonium (TPP) decorated porphyrin-based nMOFs (Zr-TCPP(TPP)/R837@M) using 4T1 cell membrane coating and R837 loading (Fig. 10A) [56]. The TEM images revealed a spherical Zr-TCPP (TPP)/R837@M shape with a clear core-shell structure. Additionally, the inserted high-resolution image indicated the successful coating of the 4T1 cell membrane (Fig. 10B). DCFH-DA was chosen as an indicator to determine the ROS-generating capability of Zr-TCPP(TPP)/R837@M, and a bright green fluorescent signal could be detected in Zr-TCPP (TPP)/R837@M + US group. Therefore, porphyrin-based nMOFs are qualified sonosensitizers (Fig. 10C). Then, the Zr-TCPP(TPP)/R837 and Zr-TCPP(TPP)/R837@M biodistribution were evaluated using an IVIS system. The results detected an evident accumulation of Zr-TCPP (TPP)/R837@M in tumors due to the tumor cell membrane coating. In contrast, Zr-TCPP(TPP)/R837 group had much lower fluorescence intensity (Fig. 10D). SDT can promote anti-tumor immune response by inducing ICD. Furthermore, the released TAAs can behave vaccine-like to activate DCs maturation. Additionally, the loaded immune adjuvants R837 in Zr-TCPP(TPP)/R837@M could induce DC maturation ($CD86^+$ $CD80^+$) and elicit a boosting immune response (Fig. 10E). Mice were implanted with 4T1 cells on their right sides as the primary tumor to assess the *in vivo* tumor-killing ability of Zr-TCPP(TPP)/R837@M combining ICB therapy. In contrast, the metastatic tumor was established on the other side one week later. The treatment scheme is represented in Fig. 10F. The *in vivo* studies revealed that Zr-TCPP (TPP)/R837@M with aCTLA-4 could eliminate local progression and suppress distal tumor growth with a 61.4% volume reduction rate. The representative flow cytometry plots also depicted a much higher $CD8^+$ T cell proportion in the SDT/ICB treatment group and a much lower presence of $Foxp3^+$ Tregs than in other groups (Fig. 10G and H). This trial primarily used the TPP decoration for mitochondria-targeting purposes to improve the $^1O_2$ oxidation effect, while the conjugated R837 was a DC maturation stimulator. The 4T1 cell membrane coating ensures the tumor-targeting ability of the nanoplatform. A tumor rechallenge model was established to confirm immune memory cell expression by Zr-TCPP(TPP)/R837@M plus aCTLA-4.

5. Conclusions and future perspectives

Since the distal metastasis and local recurrence of tumors are the leading causes of death, reversing the immunosuppressive state of the TME and reactivating host immune function could be an effective anti-tumor strategy. Over the past decade, SDT has attracted more attention as a promising alternative approach for PDT due to its inherent high penetration for deep-seated therapies and better bio-safety profile with significant tumor-killing efficacy. Furthermore, ICB therapy provides remarkable therapeutic outcomes in clinical practice. However, the frequent drug resistance and severe patient adverse events hampered its

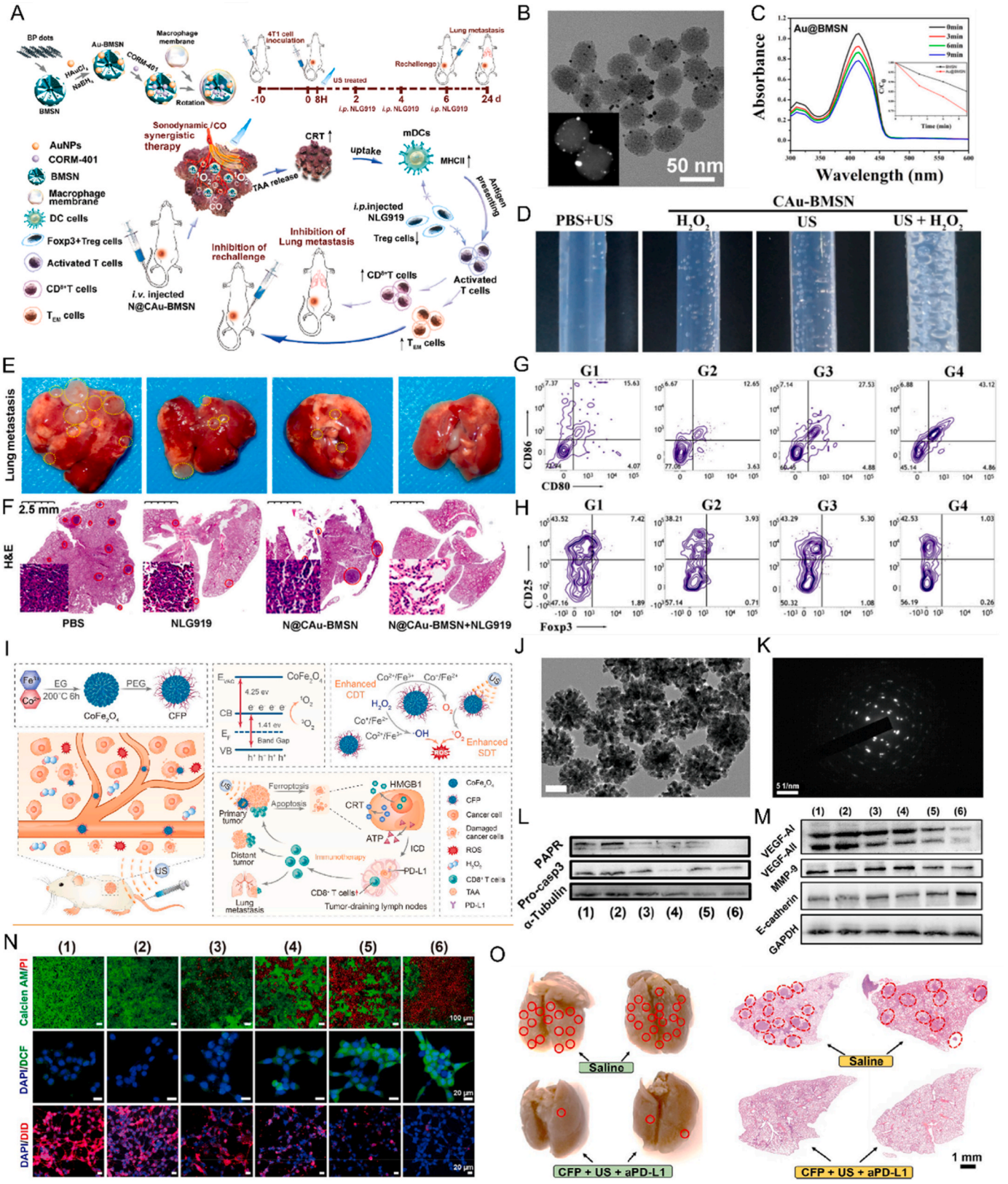

(caption on next page)

Fig. 9. (A) The schematic depiction of the prepared biomimetic nanosystem N@CAu-BMSNs. The sonodynamic/CO/IDO inhibitor (NLG919) provides synergistic therapy to suppress tumor growth, relapse, and lung metastasis. (B) TEM and STEM HAADF images of Au-BMSNs. (C) The absorbance of DPBF (100 μM) after decomposition using generated ROS from Au-BMSNs upon US triggering (1 MHz, 1 W/cm^2) at different times. The inset figure is the normalized DPBF absorbance at 415 nm after decomposition in BMSNs or Au-BMSNs using ROS generation under US triggering at different times. (D) The images of bubble generation of CO gas after US triggering in CAu-BMSNs with or without H_2O_2 (1 mM). The representative pictures (E) and H&E staining (F) of lung tissues after receiving various treatments on the 24th day. (G) DC maturation induced in tumor-draining lymph nodes on 4T1-bearing mice possessing indicated treatments. (H) The representative FACS plots depict percentages (gated on CD4$^+$ cells) of CD25$^+$ Foxp3$^+$T cells in primary tumors after receiving various indicative treatments. Reproduced with permission from Ref. [54]. Copyright 2020, American Chemical Society. (I) A schematic illustration of the synthetic CFP procedure and its acting mechanism for augmented sonodynamic and chemodynamic combination therapy by eliciting a robust immune response. (J) High-magnification TEM images of CFP. (K) The SEAD pattern of CFP. (L) Western blotting describes the expression levels of PARP and pro-caspase3 in 4T1 cells after diversified administrations. (M) Western blotting demonstrates the VEGF, MMP-9, and *E*-cadherin expression levels in 4T1 cells across different groups. The groups were assigned as (1) blank, (2) US + H_2O_2, (3) CFP, (4) CFP + H_2O_2, (5) CFP + US, and (6) CFP + H_2O_2 + US. (N) The confocal microscopy of 4T1 tumor cells after differentiated administrations and labeled using calcein AM/PI to indicate cell viability. DAPI/DCFH-DA helped detect intracellular ROS levels, and DAPI/DID assessed the integrity of the cytoplasmic membrane. (O) The representative images and H&E staining of lung tissues from saline or "CFP + US + aPD-L1" groups on day 21. Reproduced with permission from Ref. [55]. Copyright 2021, American Chemical Society.

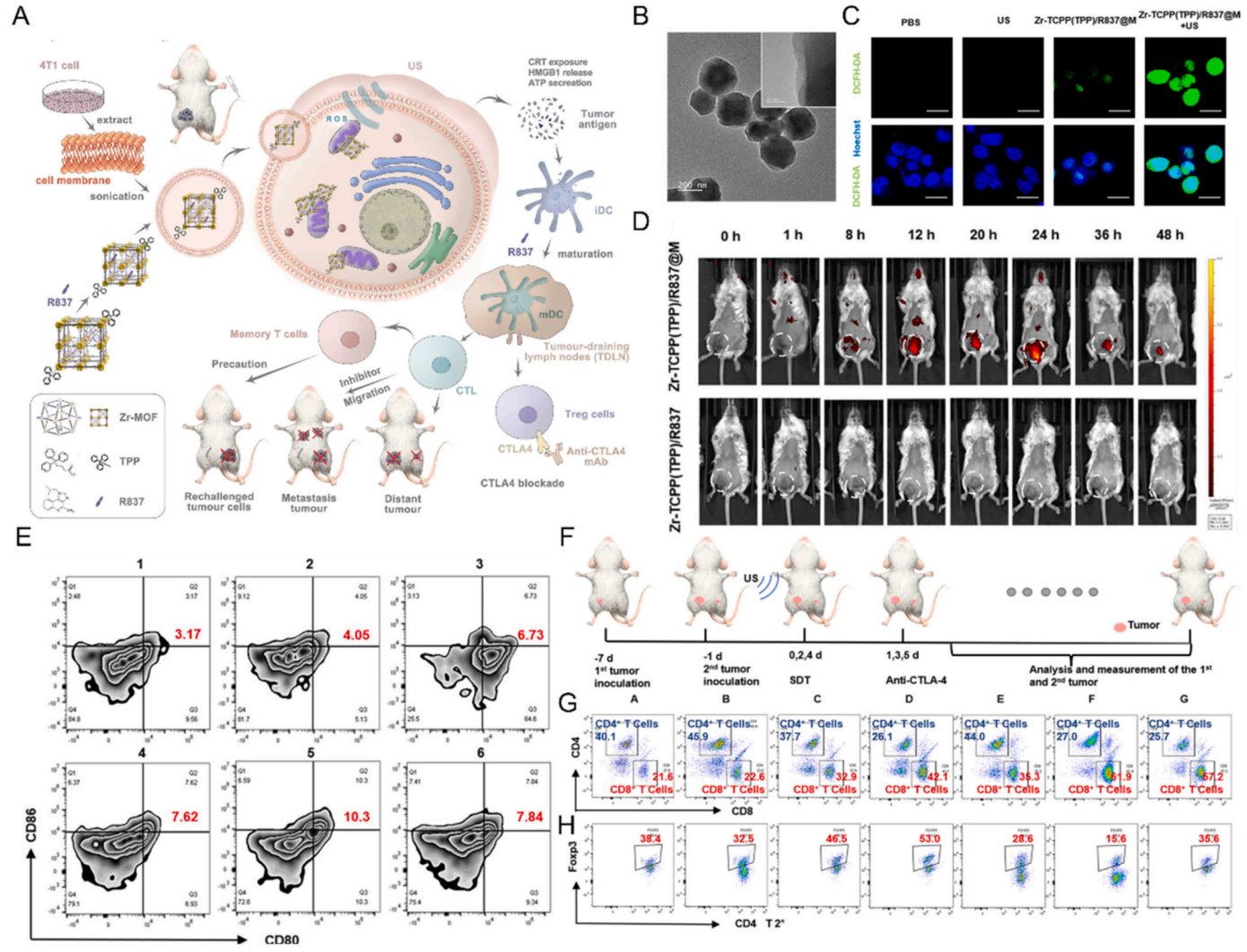

Fig. 10. (A) The schematic illustration mechanism of mitochondria-targeted cancer cell membrane-biomimetic MOF-mediated SDT and immune checkpoint blockade immunotherapy. (B) The High-resolution TEM image of Zr-TCPP(TPP)/R837@M. (C) CLSM images of 4T1 cells after being treated with Zr-TCPP(TPP)/R837@M, with or without US irradiation. DCFH-DA (10 μM) was incorporated as the intracellular ROS sensor. (D) The fluorescence images reveal the Zr-TCPP (TPP)/R837 and Zr-TCPP(TPP)/R837@M biodistribution after intravenous injection into 4T1-tumor-bearing mice at indicated time points *in vivo*. White circles indicate tumors. (E) DC maturation in the tumor-draining lymph nodes caused by various treatments on mice bearing 4T1 tumors. (F) The schematic illustration of the experiment design. (G) The representative flow cytometry plots indicate different T cell types in secondary tumors from various mice groups. Reproduced with permission from Ref. [56]. Copyright 2022 Springer Nature.

wide application. Although the monotherapy for each modality could be challenging, the combination strategy of SDT and ICB therapies can overcome the disadvantages and synergistically eliminate tumors and distal metastasis. This could provide an efficient immune memory while preventing relapse.

Despite significant preclinical trial advancements, several issues

must be addressed to expedite future clinical translations.

Firstly, the underlying mechanism of SDT is multi-factorial and remains vague. Thus, individual contributions of acoustic cavitation, SL, and pyrolysis should be studied to guide future sonosensitizer designs.

Secondly, current organic sonosensitizers have heavily depended on repositioning well-known photosensitizers. Therefore, various sonosensitizers face challenges, such as unsatisfactory ROS QY, modification difficulties, short retention time, or undesirable biocompatibility. Thus, developing novel sonosensitizers is highly needed to expand the existing categories. More strategies can rationally solve the defects. These ideas include generating extra micro-bubbles for improved acoustic cavitation, loading agents to deplete GSH level and augment ROS production, or coating with tumor membrane and antigens to enhance biocompatibility and targeting ability.

Third, the long-term biosafety of nanoplatform-based sonosensitizers is critical to early clinical translation. The most used methods in preclinical trials include cytotoxicity tests, histopathological and serological analysis, organ biodistribution, and liver and kidney function assessment. These experiments could test the short-term biosafety profile to some extent. However, minimal attention was paid to the profound intravital metabolism effects of various nano-sonosensitizers. Thus, observing the long-term physiological indexes of the treatment group is recommended. Moreover, based on the heterogeneity, animal models other than mice can fortify biosafety.

Fourth, most trials did not explain choosing specific irradiation doses of US parameters. Additionally, different US parameters made it challenging to compare the ROS-generating efficacy of each sonosensitizer. Therefore, organizing standards to optimize treatment outcomes by studying US parameters is essential.

Fifth, efforts should be made to establish if other pathways related to cell death are involved in SDT, such as autophagy, ferroptosis, and pyroptosis. More evidence can help explore their potential influence on SDT sonoactivity.

Sixth, improving tumor models is essential to evaluate the SDT effect and other treatment modalities. The ideal tumor model should be infinitely close to the real TME in the human body. US possesses a stronger tissue penetrating ability than light in PDT. However, currently utilized tumor models are superficially implanted on the body surface of mice. These models cannot highlight the advantages of US activation or analyze the influence of energy dissipation depth. In addition, assessing the therapeutic effect is difficult due to the significant differences between human tumors and the post-implantation model. Therefore, better tumor models with better clinical relevance should be established. This includes patient-derived tumor xenograft mice models to preserve the tumor heterogeneity and associated activities of various pathways.

Seventh, Table 1 depicts many ICIs used in SDT + ICB trials are intravenously or intraperitoneally injected, leading to less tumor accumulation and potential adverse effects. Therefore, ICIs should be loaded into the internal space of nanomaterials or linked on the surface using chemical bonds in future experiments to achieve targeted delivery and controllable release. This could enhance tumor-killing effects and decrease adverse effects.

Eighth, tumors can require resistance against ICB therapy, such as the loss-of-function mutations in B2M or physical myofiber barrier caused by TGF-β preventing T cell migration. Therefore, simultaneously blocking multiple immune checkpoint pathways or offering immune stimulants can regulate other signaling pathways and reduce drug resistance. Additionally, more immune checkpoint targets and related inhibitors should be explored. Most preclinical studies have utilized antibodies targeting familiar immune checkpoints. The effect of combining SDT with inhibitors targeting other pathways, such as LAG3, TIGIT, and TIM3, is worth investigating.

Ninth, the large-scale production technology of complex nanoplatform-based sonosensitizers and reducing costs can facilitate early clinical transformation using this strategy. Although most nano-sonosensitizers are novel in design and depict significant efficacy in experiments *in vivo*, it is challenging to achieve mass assembly due to difficulties in synthesis and unacceptable ICI cost. Future studies should focus on the easy-to-produce design or reduce the cost so that more patients could benefit from the treatment.

Finally, cancer development involves genetic and epigenetic dysregulation, a critical factor driving tumor initiation and progression by impacting all cancer hallmarks. Nanomaterials for targeting epigenetic changes in DNA (e.g., 5-methylcytosine) [203], RNA (e.g., N6-methyladenosine) [204–206], or protein (e.g., ubiquitination) [207] within cancer cells (named the "nano-epidrug") could be a promising strategy for enhancing immunotherapy [208]. Combining with ICB during hematological malignancies or solid tumors could overcome drug resistance or improve phototherapy [209–211]. Therefore, researchers should rationally explore new sonosensitizers or enhance the efficacy of existing nanosonosensitizers combined with ICB by targeting epigenetic modifications or linked pathways.

In summary, NPs-based SDT demonstrated a promising tumor-killing effect as PDT but possesses multiple advantages, such as better penetrating ability and safety profile. Combined with ICIs, such SDT/immunotherapy modality can synergistically target various solid tumors, causing a long-term immune memory while preventing relapse. The monotherapy drawbacks are compensated, and an even more powerful tumor-killing efficacy is achieved based on "1 + 1 > 2". However, many shortcomings still exist in SDT/ICB treatment modality. Future studies can improve these defects to accelerate clinical transformation.

Author contributions

F. Y. and Y. L. provides the idea. X. D. wrote the original manuscript; X. D. and Y. D. organize the pictures and table. Y. L. and F. Y. reviewed the final manuscript.

Declaration of competing interest

The authors declare that they have no known competing financial interests or personal relationships that could have appeared to influence the work reported in this paper.

Data availability

No data was used for the research described in the article.

Acknowledgments

This work was financially supported by the National Natural Science Foundation of China (82170154, 91959201), the Open Project Program of State Key Laboratory of Inorganic Synthesis and Preparative Chemistry (No. 2023-10).

References

[1] Z. Cheng, et al., Nanomaterials for cancer therapy: current progress and perspectives, J. Hematol. Oncol. 14 (1) (2021) 85, https://doi.org/10.1186/s13045-021-01096-0.
[2] R. Alzeibak, et al., Targeting immunogenic cancer cell death by photodynamic therapy: past, present and future, J Immunother Cancer 9 (1) (2021), https://doi.org/10.1136/jitc-2020-001926.
[3] H. Bian, et al., Tailored engineering of novel xanthonium polymethine dyes for synergetic PDT and PTT triggered by 1064 nm laser toward deep-seated tumors, Small 17 (21) (2021), e2100398, https://doi.org/10.1002/smll.202100398.
[4] J.M. DeWitt, et al., Phase 1 study of EUS-guided photodynamic therapy for locally advanced pancreatic cancer, Gastrointest. Endosc. 89 (2) (2019) 390–398, https://doi.org/10.1016/j.gie.2018.09.007.
[5] Y. Zhang, et al., Multifunctional nanoparticles as photosensitizer delivery carriers for enhanced photodynamic cancer therapy, Mater. Sci. Eng., C 115 (2020), 111099, https://doi.org/10.1016/j.msec.2020.111099.
[6] B. Yuan, et al., A self-degradable supramolecular photosensitizer with high photodynamic therapeutic efficiency and improved safety, Angew Chem. Int. Ed. Engl. 60 (2) (2021) 706–710, https://doi.org/10.1002/anie.202012477.

[7] Y. Wang, et al., Cancer-cell-activated in situ synthesis of mitochondria-targeting AIE photosensitizer for precise photodynamic therapy, Angew Chem. Int. Ed. Engl. 60 (27) (2021) 14945–14953, https://doi.org/10.1002/anie.202017350.

[8] J. Zhao, et al., Insight into the efficiency of oxygen introduced photodynamic therapy (PDT) and deep PDT against cancers with various assembled nanocarriers, Wiley Inter. Rev Nanomed Nanobiotechnol 12 (1) (2020) e1583, https://doi.org/10.1002/wnan.1583.

[9] T. Wu, et al., Engineering macrophage exosome disguised biodegradable nanoplatform for enhanced sonodynamic therapy of glioblastoma, Adv. Mater. 34 (15) (2022), e2110364, https://doi.org/10.1002/adma.202110364.

[10] Y. Liu, et al., Boosting antitumor sonodynamic therapy efficacy of black phosphorus via covalent functionalization, Adv. Sci. 8 (20) (2021), e2102422, https://doi.org/10.1002/advs.202102422.

[11] H. Hu, et al., Emerging nanomedicine-enabled/enhanced nanodynamic therapies beyond traditional photodynamics, Adv. Mater. 33 (12) (2021), e2005062, https://doi.org/10.1002/adma.202005062.

[12] S. Liang, et al., Recent advances in nanomaterial-assisted combinational sonodynamic cancer therapy, Adv. Mater. 32 (47) (2020), e2003214, https://doi.org/10.1002/adma.202003214.

[13] R. Canaparo, et al., The promising interplay between sonodynamic therapy and nanomedicine, Adv. Drug Deliv. Rev. 189 (2022), 114495, https://doi.org/10.1016/j.addr.2022.114495.

[14] Y. Zhang, et al., Advanced biotechnology-assisted precise sonodynamic therapy, Chem. Soc. Rev. 50 (20) (2021) 11227–11248, https://doi.org/10.1039/d1cs00403d.

[15] T. Yamaguchi, et al., Current landscape of sonodynamic therapy for treating cancer, Cancers 13 (24) (2021), https://doi.org/10.3390/cancers13246184.

[16] J.R. Du, et al., Recent advances in sonodynamic immunotherapy, J. Cancer Res. Clin. Oncol. (2022), https://doi.org/10.1007/s00432-022-04190-z.

[17] X. Li, Y. Zhen, S. Li, Review on combination strategy of immune checkpoint blockade, photodynamic therapy and nanomedicine against solid tumor, Mater. Des. 209 (2021), https://doi.org/10.1016/j.matdes.2021.109958.

[18] A. Ahmed, S.W.G. Tait, Targeting immunogenic cell death in cancer, Mol. Oncol. 14 (12) (2020) 2994–3006, https://doi.org/10.1002/1878-0261.12851.

[19] X. Duan, C. Chan, W. Lin, Nanoparticle-mediated immunogenic cell death enables and potentiates cancer immunotherapy, Angew Chem. Int. Ed. Engl. 58 (3) (2019) 670–680, https://doi.org/10.1002/anie.201804882.

[20] L. Minute, et al., Cellular cytotoxicity is a form of immunogenic cell death, J Immunother Cancer 8 (1) (2020), https://doi.org/10.1136/jitc-2019-000325.

[21] Y. Zhang, et al., Oxygen-carrying nanoparticle-based chemo-sonodynamic therapy for tumor suppression and autoimmunity activation, Biomater. Sci. 9 (11) (2021) 3989–4004, https://doi.org/10.1039/d1bm00198a.

[22] Y. Li, et al., Ablation of gap junction protein improves the efficiency of nanozyme-mediated catalytic/starvation/mild-temperature photothermal therapy, Adv. Mater. 35 (22) (2023), https://doi.org/10.1002/adma.202210464.

[23] S. Peng, et al., EGFR-TKI resistance promotes immune escape in lung cancer via increased PD-L1 expression, Mol. Cancer 18 (1) (2019) 165, https://doi.org/10.1186/s12943-019-1073-4.

[24] B. Zhou, et al., Hepatoma cell-intrinsic TLR9 activation induces immune escape through PD-L1 upregulation in hepatocellular carcinoma, Theranostics 10 (14) (2020) 6530–6543, https://doi.org/10.7150/thno.44417.

[25] M. Yassin, et al., Upregulation of PD-1 follows tumour development in the AOM/DSS model of inflammation-induced colorectal cancer in mice, Immunology 158 (1) (2019) 35–46, https://doi.org/10.1111/imm.13093.

[26] W. Um, et al., Recent advances in nanomaterial-based augmented sonodynamic therapy of cancer, Chem. Commun. 57 (23) (2021) 2854–2866, https://doi.org/10.1039/d0cc07750j.

[27] F. Dammeijer, et al., The PD-1/PD-L1-checkpoint restrains T cell immunity in tumor-draining lymph nodes, Cancer Cell 38 (5) (2020) 685–700 e8, https://doi.org/10.1016/j.ccell.2020.09.001.

[28] M. Tekguc, et al., Treg-expressed CTLA-4 depletes CD80/CD86 by trogocytosis, releasing free PD-L1 on antigen-presenting cells, Proc. Natl. Acad. Sci. U. S. A. 118 (30) (2021), https://doi.org/10.1073/pnas.2023739118.

[29] M. Esmaily, et al., Blockade of CTLA-4 increases anti-tumor response inducing potential of dendritic cell vaccine, J. Contr. Release 326 (2020) 63–74, https://doi.org/10.1016/j.jconrel.2020.06.017.

[30] W. Yue, et al., Checkpoint blockade and nanosonosensitizer-augmented noninvasive sonodynamic therapy combination reduces tumour growth and metastases in mice, Nat. Commun. 10 (1) (2019) 2025, https://doi.org/10.1038/s41467-019-09760-3.

[31] X. Lin, et al., Biomimetic nanoprobe-augmented triple therapy with photothermal, sonodynamic and checkpoint blockade inhibits tumor growth and metastasis, J. Nanobiotechnol. 20 (1) (2022) 80, https://doi.org/10.1186/s12951-022-01287-y.

[32] Z. Yang, et al., Perfluorocarbon loaded fluorinated covalent organic polymers with effective sonosensitization and tumor hypoxia relief enable synergistic sonodynamic-immunotherapy, Biomaterials 280 (2022), 121250, https://doi.org/10.1016/j.biomaterials.2021.121250.

[33] J. Chen, et al., Cavitation assisted endoplasmic reticulum targeted sonodynamic droplets to enhanced anti-PD-L1 immunotherapy in pancreatic cancer, J. Nanobiotechnol. 20 (1) (2022) 283, https://doi.org/10.1186/s12951-022-01459-w.

[34] J. Jeon, et al., Chemiluminescence resonance energy transfer-based immunostimulatory nanoparticles for sonoimmunotherapy, Biomaterials 283 (2022), 121466, https://doi.org/10.1016/j.biomaterials.2022.121466.

[35] W. Um, et al., Necroptosis-inducible polymeric nanobubbles for enhanced cancer sonoimmunotherapy, Adv. Mater. 32 (16) (2020), e1907953, https://doi.org/10.1002/adma.201907953.

[36] P. Wu, et al., Focused acoustic vortex-regulated composite nanodroplets combined with checkpoint blockade for high-performance tumor synergistic therapy, ACS Appl. Mater. Interfaces 14 (27) (2022) 30466–30479, https://doi.org/10.1021/acsami.2c02137.

[37] J. Huang, et al., Nanodrug with dual-sensitivity to tumor microenvironment for immuno-sonodynamic anti-cancer therapy, Biomaterials 269 (2021), 120636, https://doi.org/10.1016/j.biomaterials.2020.120636.

[38] Q. Jiang, et al., A hydrogen peroxide economizer for on-demand oxygen production-assisted robust sonodynamic immunotherapy, Theranostics 12 (1) (2022) 59–75, https://doi.org/10.7150/thno.64862.

[39] Y. Tan, et al., Nanobubbles containing sPD-1 and Ce6 mediate combination immunotherapy and suppress hepatocellular carcinoma in mice, Int. J. Nanomed. 16 (2021) 3241–3254, https://doi.org/10.2147/IJN.S305857.

[40] F. Xie, et al., Self-delivering nanodrugs developed via small-molecule-directed assembly and macrophage cloaking for sonodynamic-augmented immunotherapy, Adv. Healthcare Mater. (2022), e2102770, https://doi.org/10.1002/adhm.202102770.

[41] M. Li, et al., Acoustic triggered nanobomb for US imaging guided sonodynamic therapy and activating antitumor immunity, Drug Deliv. 29 (1) (2022) 2177–2189, https://doi.org/10.1080/10717544.2022.2095058.

[42] H. Tian, et al., Manganese-phenolic nanoadjuvant combines sonodynamic therapy with cGAS-STING activation for enhanced cancer immunotherapy, Nano Today 43 (2022), https://doi.org/10.1016/j.nantod.2022.101405.

[43] G. Wan, et al., Gene augmented nuclear-targeting sonodynamic therapy via Nrf2 pathway-based redox balance adjustment boosts peptide-based anti-PD-L1 therapy on colorectal cancer, J. Nanobiotechnol. 19 (1) (2021) 347, https://doi.org/10.1186/s12951-021-01094-x.

[44] J. Ren, et al., Ultrasound (US)-activated redox dyshomeostasis therapy reinforced by immunogenic cell death (ICD) through a mitochondrial targeting liposomal nanosystem, Theranostics 11 (19) (2021) 9470–9491, https://doi.org/10.7150/thno.62984.

[45] S. Bai, et al., Nanotransferrin-based programmable catalysis mediates three-pronged induction of oxidative stress to enhance cancer immunotherapy, ACS Nano (2021), https://doi.org/10.1021/acsnano.1c08619.

[46] Z. Zeng, et al., Activatable cancer sono-immunotherapy using semiconducting polymer nanobodies, Adv. Mater. 34 (28) (2022), e2203246, https://doi.org/10.1002/adma.202203246.

[47] J. Li, et al., Precision cancer son-immunotherapy using deep-tissue activatable semiconducting polymer immunomodulatory nanoparticles, Nat. Commun. 13 (1) (2022) 4032, https://doi.org/10.1038/s41467-022-31551-6.

[48] H. Lei, et al., Immunosonodynamic therapy designed with activatable sonosensitizer and immune stimulant imiquimod, ACS Nano (2022), https://doi.org/10.1021/acsnano.2c03395.

[49] H. Nesbitt, et al., Sonodynamic therapy complements PD-L1 immune checkpoint inhibition in a murine model of pancreatic cancer, Cancer Lett. 517 (2021) 88–95, https://doi.org/10.1016/j.canlet.2021.06.003.

[50] X. Tan, et al., Transformable nanosensitizer with tumor microenvironment-activated sonodynamic process and calcium release for enhanced cancer immunotherapy, Angew Chem. Int. Ed. Engl. 60 (25) (2021) 14051–14059, https://doi.org/10.1002/anie.202102703.

[51] X. Wei, et al., Homology and immune checkpoint dual-targeted sonocatalytic nanoagents for enhancing sonodynamic tumor therapy, ACS Appl. Mater. Interfaces 13 (28) (2021) 32810–32822, https://doi.org/10.1021/acsami.1c08105.

[52] M. Wang, et al., A multifunctional nanovaccine based on L-arginine-loaded black mesoporous titania: ultrasound-triggered synergistic cancer sonodynamic therapy/gas therapy/immunotherapy with remarkably enhanced efficacy, Small 17 (6) (2021), e2005728, https://doi.org/10.1002/smll.202005728.

[53] X. Lin, et al., Nanosonosensitizer-augmented sonodynamic therapy combined with checkpoint blockade for cancer immunotherapy, Int. J. Nanomed. 16 (2021) 1889–1899, https://doi.org/10.2147/IJN.S290796.

[54] D. Zhang, et al., Ultrasound-driven biomimetic nanosystem suppresses tumor growth and metastasis through sonodynamic therapy, CO therapy, and indoleamine 2,3-dioxygenase inhibition, ACS Nano 14 (7) (2020) 8985–8999, https://doi.org/10.1021/acsnano.0c03833.

[55] S. Fu, et al., Catalytically active CoFe2O4 nanoflowers for augmented sonodynamic and chemodynamic combination therapy with elicitation of robust immune response, ACS Nano (2021), https://doi.org/10.1021/acsnano.1c03128.

[56] J. Luo, et al., Enhancement of antitumor immunotherapy using mitochondria-targeted cancer cell membrane-biomimetic MOF-mediated sonodynamic therapy and checkpoint blockade immunotherapy, J. Nanobiotechnol. 20 (1) (2022) 228, https://doi.org/10.1186/s12951-022-01453-2.

[57] Q. Xu, et al., Manganese porphyrin-based metal-organic framework for synergistic sonodynamic therapy and ferroptosis in hypoxic tumors, Theranostics 11 (4) (2021) 1937–1952, https://doi.org/10.7150/thno.45511.

[58] Z. Kang, et al., Multifunctional theranostic nanoparticles for enhanced tumor targeted imaging and synergistic FUS/chemotherapy on murine 4T1 breast cancer cell, Int. J. Nanomed. 17 (2022) 2165–2187, https://doi.org/10.2147/IJN.S360161.

[59] C. Zhang, et al., Metal-organic framework (MOF)-Based ultrasound-responsive dual-sonosensitizer nanoplatform for hypoxic cancer therapy, Adv. Healthcare Mater. 11 (2) (2022), e2101946, https://doi.org/10.1002/adhm.202101946.

[60] E. Beguin, et al., Direct evidence of multibubble sonoluminescence using therapeutic ultrasound and microbubbles, ACS Appl. Mater. Interfaces 11 (22) (2019) 19913–19919, https://doi.org/10.1021/acsami.9b07084.

[61] Q. Tang, et al., Machine learning prediction of pyrolytic gas yield and compositions with feature reduction methods: effects of pyrolysis conditions and biomass characteristics, Bioresour. Technol. 339 (2021), 125581, https://doi.org/10.1016/j.biortech.2021.125581.

[62] S. Tsirkin, et al., Tailor-made single-core PLGA microbubbles as acoustic cavitation enhancers for therapeutic applications, ACS Appl. Mater. Interfaces 13 (22) (2021) 25748–25758, https://doi.org/10.1021/acsami.1c04770.

[63] G. Canavese, et al., Nanoparticle-assisted ultrasound: a special focus on sonodynamic therapy against cancer, Chem. Eng. J. 340 (2018) 155–172, https://doi.org/10.1016/j.cej.2018.01.060.

[64] S.M. Chowdhury, et al., Ultrasound and microbubble mediated therapeutic delivery: underlying mechanisms and future outlook, J. Contr. Release 326 (2020) 75–90, https://doi.org/10.1016/j.jconrel.2020.06.008.

[65] B. Yang, Y. Chen, J. Shi, Reactive oxygen species (ROS)-Based nanomedicine, Chem. Rev. 119 (8) (2019) 4881–4985, https://doi.org/10.1021/acs.chemrev.8b00626.

[66] J. Zhang, et al., A Self-amplifying ROS-sensitive prodrug-based nanodecoy for circumventing immune resistance in chemotherapy-sensitized immunotherapy, Acta Biomater. 149 (2022) 307–320, https://doi.org/10.1016/j.actbio.2022.06.035.

[67] P. Muhammad, et al., Carbon dots supported single Fe atom nanozyme for drug-resistant glioblastoma therapy by activating autophagy-lysosome pathway, Nano Today 45 (2022), https://doi.org/10.1016/j.nantod.2022.101530.

[68] L. Zhou, et al., Autophagy blockade synergistically enhances nanosonosensitizer-enabled sonodynamic cancer nanotherapeutics, J. Nanobiotechnol. 19 (1) (2021) 112, https://doi.org/10.1186/s12951-021-00855-y.

[69] F. Shen, et al., Immunogenic nanomedicine based on GSH-responsive nanoscale covalent organic polymers for chemo-sonodynamic therapy, Biomaterials 283 (2022), 121428, https://doi.org/10.1016/j.biomaterials.2022.121428.

[70] H. Yu, et al., ROS-responsive nano-drug delivery system combining mitochondria-targeting ceria nanoparticles with atorvastatin for acute kidney injury, Theranostics 10 (5) (2020) 2342–2357, https://doi.org/10.7150/thno.40395.

[71] N. Sharma, K. Bietar, U. Stochaj, Targeting nanoparticles to malignant tumors, Biochim. Biophys. Acta Rev. Canc 1877 (3) (2022), 188703, https://doi.org/10.1016/j.bbcan.2022.188703.

[72] Y. Zhang, et al., Macrophage-membrane-coated nanoparticles for tumor-targeted chemotherapy, Nano Lett. 18 (3) (2018) 1908–1915, https://doi.org/10.1021/acs.nanolett.7b05263.

[73] X. Zhen, P. Cheng, K. Pu, Recent advances in cell membrane-camouflaged nanoparticles for cancer phototherapy, Small 15 (1) (2019), e1804105, https://doi.org/10.1002/smll.201804105.

[74] L. Bejarano, M.J.C. Jordão, J.A. Joyce, Therapeutic targeting of the tumor microenvironment, Cancer Discov. 11 (4) (2021) 933–959, https://doi.org/10.1158/2159-8290.Cd-20-1808.

[75] G. Yang, et al., Hollow MnO(2) as a tumor-microenvironment-responsive biodegradable nano-platform for combination therapy favoring antitumor immune responses, Nat. Commun. 8 (1) (2017) 902, https://doi.org/10.1038/s41467-017-01050-0.

[76] A. Xie, et al., Stimuli-responsive Prodrug-Based Cancer Nanomedicine, vol. 56, EBioMedicine, 2020, https://doi.org/10.1016/j.ebiom.2020.102821.

[77] J. Guo, et al., Nano codelivery of oxaliplatin and folinic acid achieves synergistic chemo-immunotherapy with 5-fluorouracil for colorectal cancer and liver metastasis, ACS Nano 14 (4) (2020) 5075–5089, https://doi.org/10.1021/acsnano.0c01676.

[78] Y. Zhang, et al., A cascade nanoreactor for enhancing sonodynamic therapy on colorectal cancer via synergistic ROS augment and autophagy blockage, Nano Today 49 (2023), https://doi.org/10.1016/j.nantod.2023.101798.

[79] Y. Hu, et al., Construction of iron oxide nanoparticle-based hybrid platforms for tumor imaging and therapy, Chem. Soc. Rev. 47 (5) (2018) 1874–1900, https://doi.org/10.1039/c7cs00657h.

[80] P. Armanetti, et al., Dual photoacoustic/ultrasound multi-parametric imaging from passion fruit-like nano-architectures, Nanomedicine 14 (6) (2018) 1787–1795, https://doi.org/10.1016/j.nano.2018.05.007.

[81] Y. Liu, et al., Photothermal therapy and photoacoustic imaging via nanotheranostics in fighting cancer, Chem. Soc. Rev. 48 (7) (2019) 2053–2108, https://doi.org/10.1039/c8cs00618k.

[82] P.H. Zhao, et al., Aggregation-enhanced sonodynamic activity of phthalocyanine-artesunate conjugates, Angew Chem. Int. Ed. Engl. 61 (5) (2022), e202113506, https://doi.org/10.1002/anie.202113506.

[83] R.Y. Zhang, et al., A pH/ultrasonic dual-response step-targeting enterosoluble granule for combined sonodynamic-chemotherapy guided via gastrointestinal tract imaging in orthotopic colorectal cancer, Nanoscale 13 (7) (2021) 4278–4294, https://doi.org/10.1039/d0nr08100k.

[84] Y. Chen, et al., RNA-seq explores the mechanism of oxygen-boosted sonodynamic therapy based on all-in-one nanobubbles to enhance ferroptosis for the treatment of HCC, Int. J. Nanomed. 17 (2022) 105–123, https://doi.org/10.2147/ijn.S343361.

[85] J. Wang, et al., 'Mito-Bomb': a novel mitochondria-targeting nanosystem for ferroptosis-boosted sonodynamic antitumor therapy, Drug Deliv. 29 (1) (2022) 3111–3122, https://doi.org/10.1080/10717544.2022.2126027.

[86] Y. Zhao, et al., Platinum-titania Schottky junction as nanosonosensitizer, glucose scavenger, and tumor microenvironment-modulator for promoted cancer treatment, ACS Nano (2022), https://doi.org/10.1021/acsnano.2c02540.

[87] C.C. Yang, et al., Using C-doped TiO(2) nanoparticles as a novel sonosensitizer for cancer treatment, Antioxidants 9 (9) (2020), https://doi.org/10.3390/antiox9090880.

[88] S. Çeşmeli, C. Biray Avci, Application of titanium dioxide (TiO(2)) nanoparticles in cancer therapies, J. Drug Target. 27 (7) (2019) 762–766, https://doi.org/10.1080/1061186x.2018.1527338.

[89] F.U. Rehman, et al., Ultrasound-activated nano-TiO2 loaded with temozolomide paves the way for resection of chemoresistant glioblastoma multiforme, Cancer Nanotechnology 12 (1) (2021), https://doi.org/10.1186/s12645-021-00088-6.

[90] F. Wang, et al., Integrating Au and ZnO nanoparticles onto graphene nanosheet for enhanced sonodynamic therapy, Nano Res. 15 (10) (2022) 9223–9233, https://doi.org/10.1007/s12274-022-4599-5.

[91] Y. Liu, et al., Defect modified zinc oxide with augmenting sonodynamic reactive oxygen species generation, Biomaterials 251 (2020), 120075, https://doi.org/10.1016/j.biomaterials.2020.120075.

[92] F. Gao, et al., Titania-coated 2D gold nanoplates as nanoagents for synergistic photothermal/sonodynamic therapy in the second near-infrared window, Nanoscale 11 (5) (2019) 2374–2384, https://doi.org/10.1039/c8nr07188h.

[93] C. Li, et al., Red blood cell membrane-enveloped O(2) self-supplementing biomimetic nanoparticles for tumor imaging-guided enhanced sonodynamic therapy, Theranostics 10 (2) (2020) 867–879, https://doi.org/10.7150/thno.37930.

[94] S. Liang, et al., Intelligent hollow Pt-CuS janus architecture for synergistic catalysis-enhanced sonodynamic and photothermal cancer therapy, Nano Lett. 19 (6) (2019) 4134–4145, https://doi.org/10.1021/acs.nanolett.9b01595.

[95] X. Pan, et al., Metal-organic-framework-derived carbon nanostructure augmented sonodynamic cancer therapy, Adv. Mater. 30 (23) (2018), e1800180, https://doi.org/10.1002/adma.201800180.

[96] S. Liang, et al., Conferring Ti-based MOFs with defects for enhanced sonodynamic cancer therapy, Adv. Mater. 33 (18) (2021), e2100333, https://doi.org/10.1002/adma.202100333.

[97] J. Yao, et al., Low-intensity focused ultrasound-responsive ferrite-encapsulated nanoparticles for atherosclerotic plaque neovascularization theranostics, Adv. Sci. 8 (19) (2021), e2100850, https://doi.org/10.1002/advs.202100850.

[98] P. Xu, et al., Therapeutic effect of doxorubicin-chlorin E6-loaded mesoporous silica nanoparticles combined with ultrasound on triple-negative breast cancer, Int. J. Nanomed. 15 (2020) 2659–2668, https://doi.org/10.2147/ijn.S243037.

[99] J. An, et al., ROS-augmented and tumor-microenvironment responsive biodegradable nanoplatform for enhancing chemo-sonodynamic therapy, Biomaterials 234 (2020), 119761, https://doi.org/10.1016/j.biomaterials.2020.119761.

[100] D. Nicholas, et al., Exploiting a Rose Bengal-bearing, oxygen-producing nanoparticle for SDT and associated immune-mediated therapeutic effects in the treatment of pancreatic cancer, Eur. J. Pharm. Biopharm. 163 (2021) 49–59, https://doi.org/10.1016/j.ejpb.2021.03.005.

[101] T.G. Nguyen Cao, et al., Safe and targeted sonodynamic cancer therapy using biocompatible exosome-based nanosonosensitizers, ACS Appl. Mater. Interfaces 13 (22) (2021) 25575–25588, https://doi.org/10.1021/acsami.0c22883.

[102] P. Wu, et al., ROS-responsive blended nanoparticles: cascade-amplifying synergistic effects of sonochemotherapy with on-demand boosted drug release during SDT process, Adv. Healthcare Mater. 8 (18) (2019), e1900720, https://doi.org/10.1002/adhm.201900720.

[103] A.K. Wood, C.M. Sehgal, A review of low-intensity ultrasound for cancer therapy, Ultrasound Med. Biol. 41 (4) (2015) 905–928, https://doi.org/10.1016/j.ultrasmedbio.2014.11.019.

[104] X. Qian, Y. Zheng, Y. Chen, Micro/Nanoparticle-augmented sonodynamic therapy (SDT): breaking the depth shallow of photoactivation, Adv. Mater. 28 (37) (2016) 8097–8129, https://doi.org/10.1002/adma.201602012.

[105] B. Geng, et al., Platinum crosslinked carbon dot@TiO(2-)(x) p-n junctions for relapse-free sonodynamic tumor eradication via high-yield ROS and GSH depletion, Small 18 (6) (2022), e2103528, https://doi.org/10.1002/smll.202103528.

[106] S. Liang, et al., A robust narrow bandgap vanadium tetrasulfide sonosensitizer optimized by charge separation engineering for enhanced sonodynamic cancer therapy, Adv. Mater. 33 (36) (2021), e2101467, https://doi.org/10.1002/adma.202101467.

[107] M. Xu, et al., Sonodynamic therapy-derived multimodal synergistic cancer therapy, Cancer Lett. 497 (2021) 229–242, https://doi.org/10.1016/j.canlet.2020.10.037.

[108] S. Yamaguchi, et al., Sonodynamic therapy using water-dispersed TiO2-polyethylene glycol compound on glioma cells: comparison of cytotoxic mechanism with photodynamic therapy, Ultrason. Sonochem. 18 (5) (2011) 1197–1204, https://doi.org/10.1016/j.ultsonch.2010.12.017.

[109] Y. Zhou, et al., Construction of silica-based micro/nanoplatforms for ultrasound theranostic biomedicine, Adv. Healthcare Mater. 6 (18) (2017), https://doi.org/10.1002/adhm.201700646.

[110] X. Pan, et al., MOF-derived double-layer hollow nanoparticles with oxygen generation ability for multimodal imaging-guided sonodynamic therapy, Angew Chem. Int. Ed. Engl. 59 (32) (2020) 13557–13561, https://doi.org/10.1002/anie.202004894.

[111] T. Chen, et al., Engineered gold/black phosphorus nanoplatforms with remodeling tumor microenvironment for sonoactivated catalytic tumor theranostics, Bioact. Mater. 10 (2022) 515–525, https://doi.org/10.1016/j.bioactmat.2021.09.016.

[112] D. Sun, et al., Ultrasound-switchable nanozyme augments sonodynamic therapy against multidrug-resistant bacterial infection, ACS Nano 14 (2) (2020) 2063–2076, https://doi.org/10.1021/acsnano.9b08667.
[113] X. Wang, et al., Ultrafine titanium monoxide (TiO1+x) nanorods for enhanced sonodynamic therapy, J. Am. Chem. Soc. 142 (14) (2020) 6527–6537, https://doi.org/10.1021/jacs.9b10228.
[114] Q. Jiang, et al., Recent progress in metal–organic framework-based sonosensitizers for sonodynamic tumor therapy, Biomater. Sci. 11 (13) (2023) 4452–4470, https://doi.org/10.1039/d3bm00556a.
[115] X.J. Kong, et al., In situ porphyrin substitution in a Zr(IV)-MOF for stability enhancement and photocatalytic CO(2) reduction, Small 17 (22) (2021), e2005357, https://doi.org/10.1002/smll.202005357.
[116] M. Yuan, et al., A robust oxygen-carrying hemoglobin-based natural sonosensitizer for sonodynamic cancer therapy, Nano Lett. 21 (14) (2021) 6042–6050, https://doi.org/10.1021/acs.nanolett.1c01220.
[117] X. Jing, et al., Role of hypoxia in cancer therapy by regulating the tumor microenvironment, Mol. Cancer 18 (1) (2019) 157, https://doi.org/10.1186/s12943-019-1089-9.
[118] Y. Dong, et al., 2D piezoelectric Bi(2) MoO(6) nanoribbons for GSH-enhanced sonodynamic therapy, Adv. Mater. 33 (51) (2021), e2106838, https://doi.org/10.1002/adma.202106838.
[119] P. Zhu, Y. Chen, J. Shi, Nanoenzyme-augmented cancer sonodynamic therapy by catalytic tumor oxygenation, ACS Nano 12 (4) (2018) 3780–3795, https://doi.org/10.1021/acsnano.8b00999.
[120] Y. Xiong, et al., Engineering nanomedicine for glutathione depletion-augmented cancer therapy, Chem. Soc. Rev. 50 (10) (2021) 6013–6041, https://doi.org/10.1039/d0cs00718h.
[121] C. Shi, et al., Catalase-based liposomal for reversing immunosuppressive tumor microenvironment and enhanced cancer chemo-photodynamic therapy, Biomaterials 233 (2020), 119755, https://doi.org/10.1016/j.biomaterials.2020.119755.
[122] M. Pajares, et al., Transcription factor NFE2L2/NRF2 modulates chaperone-mediated autophagy through the regulation of LAMP2A, Autophagy 14 (8) (2018) 1310–1322, https://doi.org/10.1080/15548627.2018.1474992.
[123] W. Li, et al., Mutual-reinforcing Sonodynamic Therapy against Rheumatoid Arthritis Based on Sparfloxacin Sonosensitizer Doped Concave-Cubic Rhodium Nanozyme, vol. 276, Biomaterials, 2021, 121063, https://doi.org/10.1016/j.biomaterials.2021.121063.
[124] J. Chen, et al., Hypoxia-alleviated nanoplatform to enhance chemosensitivity and sonodynamic effect in pancreatic cancer, Cancer Lett. 520 (2021) 100–108, https://doi.org/10.1016/j.canlet.2021.07.008.
[125] P. Zhang, et al., An intelligent hypoxia-relieving chitosan-based nanoplatform for enhanced targeted chemo-sonodynamic combination therapy on lung cancer, Carbohydr. Polym. 274 (2021), 118655, https://doi.org/10.1016/j.carbpol.2021.118655.
[126] S. Dong, et al., GSH-depleted nanozymes with hyperthermia-enhanced dual enzyme-mimic activities for tumor nanocatalytic therapy, Adv. Mater. 32 (42) (2020), e2002439, https://doi.org/10.1002/adma.202002439.
[127] Y. Zhao, et al., Piezotronic effect-augmented Cu(2-x)O-BaTiO(3) sonosensitizers for multifunctional cancer dynamic therapy, ACS Nano (2022), https://doi.org/10.1021/acsnano.2c01968.
[128] J. An, et al., A pH/Ultrasound dual-response biomimetic nanoplatform for nitric oxide gas-sonodynamic combined therapy and repeated ultrasound for relieving hypoxia, Biomaterials 230 (2020), 119636, https://doi.org/10.1016/j.biomaterials.2019.119636.
[129] Y. Cao, et al., Oral nanomotor-enabled mucus traverse and tumor penetration for targeted chemo-sono-immunotherapy against colon cancer, Small (2022), e2203466, https://doi.org/10.1002/smll.202203466.
[130] M.S. Carlino, J. Larkin, G.V. Long, Immune checkpoint inhibitors in melanoma, Lancet 398 (10304) (2021) 1002–1014, https://doi.org/10.1016/s0140-6736(21)01206-x.
[131] M. Yi, et al., Synergistic effect of immune checkpoint blockade and anti-angiogenesis in cancer treatment, Mol. Cancer 18 (1) (2019) 60, https://doi.org/10.1186/s12943-019-0974-6.
[132] A.L. Heeke, A.R. Tan, Checkpoint inhibitor therapy for metastatic triple-negative breast cancer, Cancer Metastasis Rev. 40 (2) (2021) 537–547, https://doi.org/10.1007/s10555-021-09972-4.
[133] F. Passiglia, et al., Major breakthroughs in lung cancer adjuvant treatment: looking beyond the horizon, Cancer Treat Rev. 101 (2021), 102308, https://doi.org/10.1016/j.ctrv.2021.102308.
[134] H. Gonzalez, C. Hagerling, Z. Werb, Roles of the immune system in cancer: from tumor initiation to metastatic progression, Genes Dev. 32 (19–20) (2018) 1267–1284, https://doi.org/10.1101/gad.314617.118.
[135] L. Xia, et al., The cancer metabolic reprogramming and immune response, Mol. Cancer 20 (1) (2021) 28, https://doi.org/10.1186/s12943-021-01316-8.
[136] D.C. Hinshaw, L.A. Shevde, The tumor microenvironment innately modulates cancer progression, Cancer Res. 79 (18) (2019) 4557–4566, https://doi.org/10.1158/0008-5472.Can-18-3962.
[137] M. Yang, et al., The application of nanoparticles in cancer immunotherapy: targeting tumor microenvironment, Bioact. Mater. 6 (7) (2021) 1973–1987, https://doi.org/10.1016/j.bioactmat.2020.12.010.
[138] F. Antonangeli, et al., Regulation of PD-L1 expression by NF-κB in cancer, Front. Immunol. 11 (2020), 584626, https://doi.org/10.3389/fimmu.2020.584626.
[139] S.M. Toor, et al., Immune checkpoints in the tumor microenvironment, Semin. Cancer Biol. 65 (2020) 1–12, https://doi.org/10.1016/j.semcancer.2019.06.021.
[140] C. Sun, R. Mezzadra, T.N. Schumacher, Regulation and function of the PD-L1 checkpoint, Immunity 48 (3) (2018) 434–452, https://doi.org/10.1016/j.immuni.2018.03.014.
[141] L. Gandhi, et al., Pembrolizumab plus chemotherapy in metastatic non-small-cell lung cancer, N. Engl. J. Med. 378 (22) (2018) 2078–2092, https://doi.org/10.1056/NEJMoa1801005.
[142] T. Yau, et al., Nivolumab in advanced hepatocellular carcinoma: sorafenib-experienced Asian cohort analysis, J. Hepatol. 71 (3) (2019) 543–552, https://doi.org/10.1016/j.jhep.2019.05.014.
[143] J. Larkin, et al., Five-year survival with combined nivolumab and Ipilimumab in advanced melanoma, N. Engl. J. Med. 381 (16) (2019) 1535–1546, https://doi.org/10.1056/NEJMoa1910836.
[144] Q. Wu, et al., Small-molecule inhibitors, immune checkpoint inhibitors, and more: FDA-approved novel therapeutic drugs for solid tumors from 1991 to 2021, J. Hematol. Oncol. 15 (1) (2022) 143, https://doi.org/10.1186/s13045-022-01362-9.
[145] T. Kamada, et al., PD-1(+) regulatory T cells amplified by PD-1 blockade promote hyperprogression of cancer, Proc. Natl. Acad. Sci. U. S. A. 116 (20) (2019) 9999–10008, https://doi.org/10.1073/pnas.1822001116.
[146] T. Wartewig, J. Ruland, PD-1 tumor suppressor signaling in T cell lymphomas, Trends Immunol. 40 (5) (2019) 403–414, https://doi.org/10.1016/j.it.2019.03.005.
[147] J.H. Cha, et al., Mechanisms controlling PD-L1 expression in cancer, Mol. Cell 76 (3) (2019) 359–370, https://doi.org/10.1016/j.molcel.2019.09.030.
[148] Q. Peng, et al., PD-L1 on dendritic cells attenuates T cell activation and regulates response to immune checkpoint blockade, Nat. Commun. 11 (1) (2020) 4835, https://doi.org/10.1038/s41467-020-18570-x.
[149] P. Sharma, et al., Immune checkpoint therapy-current perspectives and future directions, Cell 186 (8) (2023) 1652–1669, https://doi.org/10.1016/j.cell.2023.03.006.
[150] M. Yi, et al., Combination strategies with PD-1/PD-L1 blockade: current advances and future directions, Mol. Cancer 21 (1) (2022) 28, https://doi.org/10.1186/s12943-021-01489-2.
[151] M. Gogishvili, et al., Cemiplimab plus chemotherapy versus chemotherapy alone in non-small cell lung cancer: a randomized, controlled, double-blind phase 3 trial, Nat. Med. 28 (11) (2022) 2374–2380, https://doi.org/10.1038/s41591-022-01977-y.
[152] N. Li, et al., Biomarkers related to immune checkpoint inhibitors therapy, Biomed. Pharmacother. 147 (2022), 112470, https://doi.org/10.1016/j.biopha.2021.112470.
[153] H. Lingel, M.C. Brunner-Weinzierl, CTLA-4 (CD152): a versatile receptor for immune-based therapy, Semin. Immunol. 42 (2019), 101298, https://doi.org/10.1016/j.smim.2019.101298.
[154] P. John, et al., The immune checkpoint B7x expands tumor-infiltrating Tregs and promotes resistance to anti-CTLA-4 therapy, Nat. Commun. 13 (1) (2022) 2506, https://doi.org/10.1038/s41467-022-30143-8.
[155] K. Wing, et al., CTLA-4 control over Foxp3+ regulatory T cell function, Science 322 (5899) (2008) 271–275, https://doi.org/10.1126/science.1160062.
[156] S.C. Wei, C.R. Duffy, J.P. Allison, Fundamental mechanisms of immune checkpoint blockade therapy, Cancer Discov. 8 (9) (2018) 1069–1086, https://doi.org/10.1158/2159-8290.Cd-18-0367.
[157] M.W. Rohaan, et al., Tumor-infiltrating lymphocyte therapy or Ipilimumab in advanced melanoma, N. Engl. J. Med. 387 (23) (2022) 2113–2125, https://doi.org/10.1056/NEJMoa2210233.
[158] X. Song, et al., Exposure-response analyses of tremelimumab monotherapy or in combination with durvalumab in patients with unresectable hepatocellular carcinoma, Clin. Cancer Res. 29 (4) (2023) 754–763, https://doi.org/10.1158/1078-0432.CCR-22-1983.
[159] J.D. Wolchok, et al., Overall survival with combined nivolumab and Ipilimumab in advanced melanoma, N. Engl. J. Med. 377 (14) (2017) 1345–1356, https://doi.org/10.1056/NEJMoa1709684.
[160] M. Platten, et al., Tryptophan metabolism as a common therapeutic target in cancer, neurodegeneration and beyond, Nat. Rev. Drug Discov. 18 (5) (2019) 379–401, https://doi.org/10.1038/s41573-019-0016-5.
[161] P. Darvin, et al., Immune checkpoint inhibitors: recent progress and potential biomarkers, Exp. Mol. Med. 50 (12) (2018) 1–11, https://doi.org/10.1038/s12276-018-0191-1.
[162] L. Zhai, et al., Immunosuppressive Ido in cancer: mechanisms of action, animal models, and targeting strategies, Front. Immunol. 11 (2020) 1185, https://doi.org/10.3389/fimmu.2020.01185.
[163] S. Bagchi, R. Yuan, E.G. Engleman, Immune checkpoint inhibitors for the treatment of cancer: clinical impact and mechanisms of response and resistance, Annu. Rev. Pathol. 16 (2021) 223–249, https://doi.org/10.1146/annurev-pathol-042020-042741.
[164] C. Liu, et al., KRAS-G12D mutation drives immune suppression and the primary resistance of anti-PD-1/PD-L1 immunotherapy in non-small cell lung cancer, Cancer Commun. 42 (9) (2022) 828–847, https://doi.org/10.1002/cac2.12327.
[165] J. Gao, et al., Loss of IFN-gamma pathway genes in tumor cells as a mechanism of resistance to anti-CTLA-4 therapy, Cell 167 (2) (2016) 397–404 e9, https://doi.org/10.1016/j.cell.2016.08.069.
[166] S. Gettinger, et al., Impaired HLA class I antigen processing and presentation as a mechanism of acquired resistance to immune checkpoint inhibitors in lung cancer, Cancer Discov. 7 (12) (2017) 1420–1435, https://doi.org/10.1158/2159-8290.Cd-17-0593.

[167] S.P. Kubli, et al., Beyond immune checkpoint blockade: emerging immunological strategies, Nat. Rev. Drug Discov. 20 (12) (2021) 899–919, https://doi.org/10.1038/s41573-021-00155-y.
[168] Q. Sui, et al., Inflammation promotes resistance to immune checkpoint inhibitors in high microsatellite instability colorectal cancer, Nat. Commun. 13 (1) (2022) 7316, https://doi.org/10.1038/s41467-022-35096-6.
[169] J. Llovet, et al., A phase Ib trial of lenvatinib (LEN) plus pembrolizumab (PEMBRO) in unresectable hepatocellular carcinoma (uHCC): updated results, Ann. Oncol. 30 (2019) v286–v287, https://doi.org/10.1093/annonc/mdz247.073.
[170] M.A. Postow, R. Sidlow, M.D. Hellmann, Immune-related adverse events associated with immune checkpoint blockade, N. Engl. J. Med. 378 (2) (2018) 158–168, https://doi.org/10.1056/NEJMra1703481.
[171] R. Kumari, D. Sunil, R.S. Ningthoujam, Hypoxia-responsive nanoparticle based drug delivery systems in cancer therapy: an up-to-date review, J. Contr. Release 319 (2020) 135–156, https://doi.org/10.1016/j.jconrel.2019.12.041.
[172] J. Fu, et al., Activatable Nanomedicine for Overcoming Hypoxia-Induced Resistance to Chemotherapy and Inhibiting Tumor Growth by Inducing Collaborative Apoptosis and Ferroptosis in Solid Tumors, vol. 268, Biomaterials, 2021, https://doi.org/10.1016/j.biomaterials.2020.120537.
[173] X. Jiao, et al., Engineering oxygen-deficient ZrO(2-x) nanoplatform as therapy-activated "immunogenic cell death (ICD)" inducer to synergize photothermal-augmented sonodynamic tumor elimination in NIR-II biological window, Biomaterials 272 (2021), 120787, https://doi.org/10.1016/j.biomaterials.2021.120787.
[174] J. Zheng, et al., Sonosensitizer nanoplatform-mediated sonodynamic therapy induced immunogenic cell death and tumor immune microenvironment variation, Drug Deliv. 29 (1) (2022) 1164–1175, https://doi.org/10.1080/10717544.2022.2058653.
[175] G.M. Cramer, K.A. Cengel, T.M. Busch, Forging forward in photodynamic therapy, Cancer Res. 82 (4) (2022) 534–536, https://doi.org/10.1158/0008-5472.CAN-21-4122.
[176] M.Y. Li, et al., Synthesis and evaluation of novel fluorinated hematoporphyrin ether derivatives for photodynamic therapy, Bioorg. Chem. 107 (2021), 104528, https://doi.org/10.1016/j.bioorg.2020.104528.
[177] H. Xu, et al., Biocompatible Fe-Hematoporphyrin coordination nanoplatforms with efficient sonodynamic-chemo effects on deep-seated tumors, Biomaterials 257 (2020), 120239, https://doi.org/10.1016/j.biomaterials.2020.120239.
[178] A. Zhou, et al., Biomimetic activator of sonodynamic ferroptosis amplifies inherent peroxidation for improving the treatment of breast cancer, Small 18 (12) (2022), e2106568, https://doi.org/10.1002/smll.202106568.
[179] J. Ding, et al., Self-activatable photo-extracellular vesicle for synergistic trimodal anticancer therapy, Adv. Mater. 33 (7) (2021), e2005562, https://doi.org/10.1002/adma.202005562.
[180] S. Kim, et al., In situ immunogenic clearance induced by a combination of photodynamic therapy and rho-kinase inhibition sensitizes immune checkpoint blockade response to elicit systemic antitumor immunity against intraocular melanoma and its metastasis, J Immunother Cancer 9 (1) (2021), https://doi.org/10.1136/jitc-2020-001481.
[181] Y. Zhao, et al., Tumor microenvironment-responsive Cu/CaCO3 -based nanoregulator for mitochondrial homeostasis disruption-enhanced chemodynamic/sonodynamic therapy, Small 18 (38) (2022), e2204047, https://doi.org/10.1002/smll.202204047.
[182] W. Li, et al., Targeting photodynamic and photothermal therapy to the endoplasmic reticulum enhances immunogenic cancer cell death, Nat. Commun. 10 (1) (2019) 3349, https://doi.org/10.1038/s41467-019-11269-8.
[183] Y. Wang, et al., Homologous targeting nanoparticles for enhanced PDT against osteosarcoma HOS cells and the related molecular mechanisms, J. Nanobiotechnol. 20 (1) (2022) 83, https://doi.org/10.1186/s12951-021-01201-y.
[184] H. Tan, et al., Tumor microenvironment pH-responsive pentagonal gold prism-based nanoplatform for multimodal imaging and combined therapy of castration-resistant prostate cancer, Acta Biomater. 141 (2022) 408–417, https://doi.org/10.1016/j.actbio.2022.01.012.
[185] Z. Gong, Z. Dai, Design and challenges of sonodynamic therapy system for cancer theranostics: from equipment to sensitizers, Adv. Sci. 8 (10) (2021), 2002178, https://doi.org/10.1002/advs.202002178.
[186] X. Yu, et al., Neutrophil camouflaged stealth nanovehicle for photothermal-induced tumor immunotherapy by triggering pyroptosis, Adv. Sci. 10 (15) (2023), e2207456, https://doi.org/10.1002/advs.202207456.
[187] Y. Yang, et al., Semiconducting polymer nanoparticles as theranostic system for near-infrared-II fluorescence imaging and photothermal therapy under safe laser fluence, ACS Nano 14 (2) (2020) 2509–2521, https://doi.org/10.1021/acsnano.0c00043.
[188] X. Wang, et al., Enhancing penetration ability of semiconducting polymer nanoparticles for sonodynamic therapy of large solid tumor, Adv. Sci. 9 (6) (2022), e2104125, https://doi.org/10.1002/advs.202104125.
[189] M. Li, M. Zhao, J. Li, Near-infrared absorbing semiconducting polymer nanomedicines for cancer therapy, WIREs Nanomed. Nanobiotechnology 15 (3) (2022), https://doi.org/10.1002/wnan.1865.
[190] W. Fan, et al., Calcium carbonate-methylene blue nanohybrids for photodynamic therapy and ultrasound imaging, Sci. China Life Sci. 61 (4) (2018) 483–491, https://doi.org/10.1007/s11427-017-9260-1.
[191] Y. Zhang, et al., Near infrared-activatable methylene blue polypeptide codelivery of the NO prodrug via π-π stacking for cascade reactive oxygen species amplification-mediated photodynamic therapy, ACS Appl. Mater. Interfaces 15 (10) (2023) 12750–12765, https://doi.org/10.1021/acsami.2c21280.
[192] Y. Li, et al., Cell penetrating peptide-modified nanoparticles for tumor targeted imaging and synergistic effect of sonodynamic/HIFU therapy, Int. J. Nanomed. 14 (2019) 5875–5894, https://doi.org/10.2147/IJN.S212184.
[193] N. Tao, et al., A cascade nanozyme with amplified sonodynamic therapeutic effects through comodulation of hypoxia and immunosuppression against cancer, ACS Nano (2021), https://doi.org/10.1021/acsnano.1c07504.
[194] M. Hasanzadeh Kafshgari, W.H. Goldmann, Insights into theranostic properties of titanium dioxide for nanomedicine, Nano-Micro Lett. 12 (1) (2020) 22, https://doi.org/10.1007/s40820-019-0362-1.
[195] S. Kwon, et al., Nanomedicines for reactive oxygen species mediated approach: an emerging paradigm for cancer treatment, Acc. Chem. Res. 52 (7) (2019) 1771–1782, https://doi.org/10.1021/acs.accounts.9b00136.
[196] A. Naldoni, et al., Photocatalysis with reduced TiO(2): from black TiO(2) to cocatalyst-free hydrogen production, ACS Catal. 9 (1) (2019) 345–364, https://doi.org/10.1021/acscatal.8b04068.
[197] Y. Luo, J. Ma, W. Lu, The significance of mitochondrial dysfunction in cancer, Int. J. Mol. Sci. 21 (16) (2020), https://doi.org/10.3390/ijms21165598.
[198] S.Y. Srinivasan, et al., Applications of cobalt ferrite nanoparticles in biomedical nanotechnology, Nanomedicine 13 (10) (2018) 1221–1238, https://doi.org/10.2217/nnm-2017-0379.
[199] J. Yang, Y.W. Yang, Metal-organic frameworks for biomedical applications, Small 16 (10) (2020), e1906846, https://doi.org/10.1002/smll.201906846.
[200] Y. Liu, Y. Zhao, X. Chen, Bioengineering of metal-organic frameworks for nanomedicine, Theranostics 9 (11) (2019) 3122–3133, https://doi.org/10.7150/thno.31918.
[201] P. Gao, et al., Antitumor agents based on metal-organic frameworks, Angew Chem. Int. Ed. Engl. 60 (31) (2021) 16763–16776, https://doi.org/10.1002/anie.202102574.
[202] Y. Pu, et al., Sono-controllable and ROS-sensitive CRISPR-cas9 genome editing for augmented/synergistic ultrasound tumor nanotherapy, Adv. Mater. 33 (45) (2021), e2104641, https://doi.org/10.1002/adma.202104641.
[203] R. Deng, et al., Targeting epigenetic pathway with gold nanoparticles for acute myeloid leukemia therapy, Biomaterials 167 (2018) 80–90, https://doi.org/10.1016/j.biomaterials.2018.03.013.
[204] K. Cao, et al., Glutathione-bioimprinted nanoparticles targeting of n6-methyladenosine fto demethylase as a strategy against leukemic stem cells, Small 18 (13) (2022), 2106558, https://doi.org/10.1002/smll.202106558.
[205] Lingxiao Zhang, et al., Hepcidin-based nanocomposites for enhanced cancer immunotherapy by modulating iron export-mediated n6-methyladenosine rna transcript, Adv. Funct. Mater. 32 (2) (2022), 2107195, https://doi.org/10.1002/adfm.202107195.
[206] Y. Du, et al., Gold nanorods exhibit intrinsic therapeutic activity via controlling n6-methyladenosine-based epitranscriptomics in acute myeloid leukemia, ACS Nano 15 (11) (2021) 17689–17704, https://doi.org/10.1021/acsnano.1c05547.
[207] Y. Yu, et al., Bortezomib-encapsulated cus/carbon dot nanocomposites for enhanced photothermal therapy via stabilization of polyubiquitinated substrates in the proteasomal degradation pathway, ACS Nano 14 (8) (2020) 10688–10703, https://doi.org/10.1021/acsnano.0c05332.
[208] Yue Song, et al., A bimetallic metal-organic framework-based biomimetic nanoplatform enhances anti-leukemia immunity via synchronizing DNA demethylation and rna hypermethylation, Adv. Mater. (2023), e2210895, https://doi.org/10.1002/adma.202210895.
[209] Y. Du, et al., Targeting n6-methyladenosine reader ythdf1 promotes second near-infrared nano-photothermal immunotherapy, Chem. Eng. J. 453 (2023), 139635, https://doi.org/10.1016/j.cej.2022.139635.
[210] J. Liu, et al., Cyclodextrin-functionalized gold nanorods loaded with meclofenamic acid for improving n(6)-methyladenosine-mediated second near-infrared photothermal immunotherapy, ACS Appl. Mater. Interfaces 14 (36) (2022) 40612–40623, https://doi.org/10.1021/acsami.2c09978.
[211] Y. Sun, et al., Decitabine-loaded gold nanocages for photothermal cancer therapy via DNA hypermethylation reversal, ACS Appl. Nano Mater. 4 (10) (2021) 10556–10564, https://doi.org/10.1021/acsanm.1c02064.